Supplementary Information for

Spectral Physical Unclonable Functions: Downscaling Randomness with Multi-Resonant Hybrid Particles

Martin Sandomirskii,[*,†] Elena Petrova,[†] Pavel Kustov,[†] Lev Chizhov,[†] Artem Larin,[†] Stéphanie Bruyère,[‡] Vitaly Yaroshenko,[†] Eduard Ageev,[†] Pavel Belov,[†,¶] and Dmitry Zuev[*,†]

†*School of Physics and Engineering, Faculty of Physics, ITMO University, Kronverksky Pr. 49, bldg. A, St. Petersburg, 197101, Russia*

‡*University of Lorraine, CNRS, IJL, F-54000 Nancy, France*

¶*School of Engineering, New Uzbekistan University, Movarounnahr str. 1, 100000, Tashkent, Uzbekistan*

E-mail: m.sandomirskii@metalab.ifmo.ru; d.zuev@metalab.ifmo.ru

Contents

Supplementary Note 1: Quantum efficiency estimations **5**

Supplementary Note 2: Quantum efficiency mapping **9**

Supplementary Note 3: On the collection efficiency of the PL signal **10**

Supplementary Note 4: Description of the processes involved in the solidification of Au/Si particles **11**

Supplementary Note 5: Grain size distribution **13**

Supplementary Note 6: On the cooling rate of liquid gold-silicon droplets **15**

Supplementary Note 7: Finding the most appropriate k value during PL map clustering **16**

Supplementary Note 8: Estimating the encoding capacity of the second PUF protocol **17**

Supplementary Note 9: On the number of possible different PL responses from one particle-based microstructure **18**

Supplementary Note 10: On the concept of One-Time Password verification **20**

Supplementary Note 11: Comparing the production and full readout times for the OTP verification token concept **22**

Supplementary Note 12: The impact of the number of spectra comparisons during verification on the OTP token's performance **23**

Supplementary Note 13: NIST testing of ML-generated embeddings **25**

Supplementary Note 14: Calculating information entropy of ML-generated embeddings **26**

Supplementary Note 15: On the encoding capacity of embedding space **27**

Supplementary Note 16: On the concept and calculation of storage density **28**

Supplementary Note 17: Calculation of the overall cost of a single PUF label **30**

Supplementary Note 18: PL measurements with an industrial optical fiber spectrometer **32**

Supplementary Note 19: On the environmental stability of proposed PL-based PUFs **33**

Supplementary Figure 1: Energy-dispersive X-ray spectroscopy (EDS) maps of cross sections of three investigated Au/Si particles **36**

Supplementary Figure 2: Size distribution of laser-fabricated hybrid Au/Si particles **37**

Supplementary Figure 3: Au/Si Photoluminescence Slopes **38**

Supplementary Figure 4: The scheme of the setup used to estimate quantum efficiency of hybrid Au/Si nanoparticles **39**

Supplementary Figure 5: Quantum efficiency estimations **40**

Supplementary Figure 6: Quantum efficiency mapping **41**

Supplementary Figure 7: Simulation of the PL radiation pattern of hybrid Au/Si particles **42**

Supplementary Figure 8: On the acquisition times necessary for obtaining low-noise PL spectra **43**

Supplementary Figure 9: Grain size distribution characterization for three different Au/Si particles **44**

Supplementary Figure 10: HRTEM images of silicon grains of Au/Si particles and their FFT analysis **45**

Supplementary Figure 11: Computer generation of our particles' internal structure for numerical simulations **46**

Supplementary Figure 12: Ranges of the field enhancement factor for different Au/Si particle models **47**

Supplementary Figure 13: A scheme summarizing the Challenge, Response, Post-processing, Key, and Validation method for the three proposed PUF protocols **48**

Supplementary Figure 14: Finding the most appropriate value of clusters prescribed during the map clustering **49**

Supplementary Figure 15: SEM imaging and high-resolution PL mapping of laser-printed QR codes **50**

Supplementary Figure 16: The process of PL image binarization made to estimate the encoding capacity of the second PUF protocol **51**

Supplementary Figure 17: Evaluating the number of possible different PL responses that can be retrieved from one laser-printed microstructure **52**

Supplementary Figure 18: Pairwise distance heatmap for the embeddings of the PL spectra measured from the same location with different pump polarizations **53**

Supplementary Figure 19: Characterizing the OTP token's performance depending on the number of spectra comparisons made during its verifications **54**

Supplementary Figure 20: Results of the calculation of entropy distributions per each embedding dimension **55**

Supplementary Figure 21: Distribution of the coordinates of all components of all embedding vectors obtained during ML model training **56**

Supplementary Figure 22: Testing an industrial optical fiber spectrometer for possible PL measurement **57**

Supplementary Figure 23: Considering the effect of the protective PDMS coating on the PL properties of the sample **58**

Supplementary Figure 24: Testing environmental stability of the PL spectra-based PUFs **59**

Supplementary Figure 25: Validation of the developed ML model **60**

Supplementary Table 1: Comparison of the quantum efficiency of silicon-based PL emitters between different works **61**

Supplementary Table 2: Summary of the randomness tests of binary sequences retrieved from the ML-generated embeddings of unique PL spectra **62**

Supplementary Table 3: The performance of several prominent optical PUFs in terms of critical and overall PUF size, storage density, encoding capacity, and acquisition time for a single optical measurement **63**

References **68**

Supplementary Note 1. Quantum efficiency estimation

Quantum efficiency (QE) of any semiconductor-based photo-emission device can be defined as the ratio of the number of emitted photons by the number of photons absorbed from the pump beam. And due to the uncertain cross section of multiphoton absorption in the investigated system, the measurement of its QE becomes rather challenging task.

Here, in order to properly evaluate QE, we have ideologically followed the approach utilized earlier in refs.[1–3] This method consists of two logical parts. First, the number of emitted and absorbed photons is experimentally estimated. Then, all corrections related to the energy losses in the measurement system are taken into account, and the QE value is calculated.

The idea for estimating the number of absorbed photons, first proposed in ref,[3] is based on the nonlinear dependence of multiphoton absorption on the excitation power density in the studied system. This means, that, under relatively low incident flux, the absorption during the laser-matter interaction is expected to be primarily linear, while at higher power densities the nonlinear component of this process should become dominant. These assumptions can be verified by studying the behavior of reflected laser light in response to changes in the pump intensity, which is presented below.

The scheme of the experimental setup used to estimate quantum efficiency of hybrid gold-silicon particles is shown in **Supplementary Fig. 4**. Here, the laser beam, travelling through a system of protected silver mirrors PF10-03-P01 and longpass dichroic beamsplitter DMLP900, is focused on the structure of interest by the 100X Mitutoyo Plan Apo NIR objective with NA=0.7. Reflected laser beam and emitted white-light signal are then collected by the same objective, filtered to attenuate the laser intensity, and, finally, processed by the Horiba LabRam HR spectrometer with thermoelectrically cooled charge-coupled device (CCD) Andor DU 420A-OE 325. When measuring the white-light spectra, shortpass filter FESH1000 was used to completely suppress the laser signal. In turn, to measure the intensity of the reflected laser, a combination of ND filters from Reflective ND Filter Kit NUK01

was set to avoid the saturation of the CCD.

As presented in **Supplementary Fig. 4**, there are multiple optical elements in the experimental setup that all contribute into the weakening of the measured signals (outlined with a green dashed line). Moreover, some of these elements (including, but not limited to, dichroic mirror, spectrometer grating, and CCD matrix) are distinguished by the strongly nonlinear dispersion of the attenuation coefficient (i.e., signal transmission efficiency). Thus, it is crucial to take into account their influence on the measured signal within the spectral range of interest: 400–1100 nm. In order to do so, a calibration curve of the experimental system was quantified in three stages.

1. The AvaLight-HAL-CAL-Mini broadband light source was installed in the experimental setup and its light beam was transmitted through the optical fiber, several silver mirrors, and the additional objective to the front end of the 100x objective, shown in **Supplementary Fig. 4**.

2. A combination of shortpass (FESH) and longpass (FELH) filters was set in the path of the light beam in order to achieve a narrow wavelength range with a width of no more than 50 nm.

3. The mean power of the obtained beam was evaluated by the power meter (Ophir, Nova II) with 3A thermal sensor before the 100x objective, and the "power–counts" conversion coefficient was calculated using the corresponding signal measured by the spectrometer.

The second and the third points were performed for different central wavelengths with a step not higher than 50 nm in the range of 400–900 nm. The same logic was used to obtain the relative attenuation coefficient at the laser line wavelength. The resulted smoothed and normalized calibration curve, showing the relative efficiency of converting photons (collected by the objective) into units of the spectrometer scale, is inserted in **Supplementary Fig. 4**. These attenuation data were further used to correctly evaluate the number of photons, emitted or absorbed by the investigated Au/Si structures.

For our investigations, three different Au/Si particles with effective transverse sizes of 520

nm, 500 nm, and 790 nm, were chosen. For each of them, **Supplementary Fig. 5** shows the measured white-light spectra (a–c) and reflected laser intensity (d–f) dependencies on the incident laser fluence. In all experiments, at low excitation power densities the relationship between the integrated intensity of the reflected laser and the pump flux is clearly linear. This confirms that the energy characteristics of the physical processes involved here (the scattering/absorption cross-section and, directly, the reflectivity of the sample itself) do not depend on the excitation power density. But at higher laser fluences, deviation from this proportional dependence is observed for each structure. Here, the nonlinear optical absorption is greatly enhanced and prevails over the linear part. Consequently, the number of photons absorbed in the system at given laser fluence $N^m_{abs_i}$ can be estimated as the difference between the reflected laser intensity calculated by linear extrapolation of the investigated dependence and the measured one (indicated by green arrows in **Supplementary Fig. 5d–f**).

In parallel, the number of photons emitted by each structure and measured by our spectrometer $N^m_{em_i}$ can be found by integrating the corresponding photoluminescence spectrum over the whole visible and near-infrared range.

After taking into account the measured signal attenuation function (using the formula $N_i = N^m_i/\alpha$), the numbers of photons absorbed and emitted by each structure were found to be: $N_{abs_1} = 2{,}4 \cdot 10^9$ and $N_{em_1} = 2{,}7 \cdot 10^6$; $N_{abs_2} = 4{,}0 \cdot 10^9$ and $N_{em_2} = 3{,}6 \cdot 10^6$; $N_{abs_3} = 4{,}5 \cdot 10^9$ and $N_{em_3} = 1{,}8 \cdot 10^6$.

Finally, we can calculate the desired QE as follows:

$$\eta = \frac{N_{em}}{\beta N_{abs}}, \tag{1}$$

where $\beta \approx 0.065$ — the efficiency of PL collection by an objective with NA = 0.75 used in our experiments (see **Supplementary Note 3** for more information). Resulted values are following: $\eta_1 = 1{,}73\%$, $\eta_2 = 1{,}38\%$, $\eta_3 = 0{,}62\%$.

Usually quantum efficiency is understood as the conversion efficiency of electron-hole pairs to photons. In this case, it is necessary to multiply the result by the order of nonlinearity of the responsible absorption process. With this in mind, one can get:

$$\eta_1^{2PA} = 3{,}46\%, \quad \eta_2^{2PA} = 2{,}76\%, \quad \eta_3^{2PA} = 1{,}24\%;$$

$$\eta_1^{3PA} = 5{,}19\%, \quad \eta_2^{3PA} = 4{,}14\%, \quad \eta_3^{3PA} = 1{,}86\%.$$

Supplementary Note 2. Quantum efficiency mapping

In addition to estimating the QE of individual particles, we also measured QE map for a structure consisting of several scattered hybrid particles (see **Supplementary Fig. 6**). To do this, actions similar to those described above (**Supplementary Note 1)** were carried out, but only at the scale of maps and not single measurements. So, a number of maps representing the intensity of the reflected laser at different incident fluences were recorded (Supplementary **Fig. 6a**). Linear extrapolation of the measured dependence was applied for each pixel of this sequence, and the difference between the estimated number of reflected photons and the one obtained at high excitation fluxes was taken as the number of absorbed photons (**Supplementary Fig. 6b**). Number of emitted photons was calculated using PL map at the same pump intensities (**Supplementary Fig. 6c**). Taking into account all the losses in the measuring setup and considering two-photon absorption as the main absorption process, one can estimate the QE map, which is presented in **Supplementary Fig. 6d**.

Supplementary Note 3. On the collection efficiency of the PL signal

One of the important parameters that strongly affects the intensity of the measured signal is the collection efficiency. It shows how much energy radiated by a particle in all directions gets into the lens aperture. In order to roughly estimate this parameter (and use the obtained values to calculate the QE), it is necessary to consider the PL radiation of the studied particles. For this, the following series of COMSOL simulations were carried out.

First, the geometry of the particle was generated, and the model took into account the dimensions of the structure, its shape, the average grain size, as well as the presence of a substrate (see **Supplementary Fig. 7**). At the same time, the position of the *c*-Si grains was set randomly using the method described in **Methods** and presented in **Supplementary Fig. 11** . Then, several ($\sim$15) coherent electric dipole (ED) emitters were set inside each grain, oriented and arranged randomly, so that the total number of dipoles inside the silicon volume was about 1000. The calculation of the field emitted by all these EDs gives an estimate of the PL radiation pattern of the generated particle at given wavelength. By considering the ratio of the energy flow through the surface corresponding to the collecting aperture to the total energy flow, one can obtain the desired estimate of the collection efficiency in the system. This value corresponds to a given radiation wavelength, therefore the average over the whole PL spectrum range (400-900 nm) should be taken.

Repetition of the described simulations for various randomly generated particles and averaging of the obtained results leads to the final value: $\beta \approx 6{,}5\%$. It should be noted, though, that due to the uniqueness of the internal structure of each of the studied particles, this estimate is rather rough and is intended only for an approximate understanding.

Supplementary Note 4. Description of the processes involved in the solidification of Au/Si particles

As we described in the main body of the article, by utilizing laser-induced dewetting of Au/Si bilayers, one can create sub-microdroplets of biatomic solution. The solidification of these hybrid beads may be outlined as a set of several successive stages.[4] First, liquid state cooling takes place, bringing the system to the liquidus temperature T_L, where l and $l+s$ states may coexist, i.e., have the same Gibbs free energy. Due to the noticeable predominance of silicon in the considered system (**Supplementary Fig. 1**), crystalline Si is supposed to form from this eutectic composition during the next steps. However, the nucleation of c-Si doesn't start immediately; it is suppressed by the nuclei equilibration processes.[5] As a result, some undercooling of the melt is assumed until the nucleation rate becomes sufficient to overpower further cooling. An important parameter in this competition is the cooling rate of the system (K). The higher the K values, the greater undercooling is required; moreover, a particular upper limit exists, above which crystallization doesn't have time to launch, and only glass transition takes place[6] (which will negatively affect the PL generation performance of the resulting system[7]). This case, though, is not the subject of consideration in our work.

Once spontaneous nucleation and the consequent growth of c-Si nanograins are initiated, the recalescence stage begins, manifested in a rapid increase in the droplet temperature due to the released enthalpy. This transient stage is distinguished by its strongly non-equilibrium nature and extremely short duration, as the system develops from the metastable state of undercooled melt back to the quasi-equilibrium liquidus level. It also should be noted that, due to the formation of solid silicon, atomic concentrations in the Au/Si eutectic composition change, thus shifting the corresponding liquidus temperature (see **Fig. 3b** in the main part of the manuscript).

When the release of latent heat of fusion ceases to exceed the external heat removal, the recalescence stage gives way to segregated solidification. Here, the growth of c-Si nanograins proceeds via the adsorption of silicon atoms from the liquid alloy, and the system evolves

along the liquidus curve down to the eutectic point. Since gold and silicon are mutually insoluble, metal atoms are forced to diffuse out of the crystallization zones to maintain chemical equilibrium, disturbed by the silicon phase transition. This process provides grain growth, yet it is found to be its main limiting factor.[6] As a result, a gold-saturated network is established around randomly developed silicon nanocrystals, which is confirmed by the high-angle annular dark field (HDAAF-STEM) images shown in **Fig. 3a** (in the main part of the manuscript). Finally, as the system approaches the solidus level, the diffusion process freezes and stops the grain growth dynamics. After complete solidification of the particle, solid-state cooling gradually returns it to thermal equilibrium with the environment.

Supplementary Note 5. Grain size distribution

Supplementary Fig. 9(d-f) illustrates the c-Si grain size distribution (GSD) for three different hybrid particles obtained in the experiments. These data were extracted from the cross-sectional STEM images of the particles (see **Supplementary Fig. 9(a-c)**) and they represent some statistical distribution that is close in shape to the logarithmic-normal one.[8] A comprehensive study of the problem of random grain nucleation and growth conducted by Bill and Bergmann[9] explains the reason for this similarity. Motivated by the Kolmogorov-Avrami-Mehl-Johnson (KAMJ) model,[10] authors analytically derived the formula describing the GSD inside an arbitrary crystallized volume:[9]

$$N(g) = \left(\frac{I_0}{v_0}\right)\left(\frac{g_{inf}}{g_c}\right)\left(\frac{g_c}{g}\right)^d \exp\left[(-1)^d\left(\frac{\ln\frac{g}{g_{inf}}}{\frac{t_{cI}}{t_{cv}}}\right)^{d+1}\right]\Theta\left(\frac{g_{inf}-g}{v_0 t_{cv}}\right), \tag{2}$$

where g and g_c are the grain size and critical size, respectively; $g_{inf} = v_0 t_{cv}$; I_0 and v_0 are the constant microscopic nucleation and growth rates; t_{cI} and t_{cv} are decay times for these processes (determining their characteristic duration); $d = 3$ is the dimension of the crystallization process; Θ is the Heaviside function. Based on this formula, we carried out the many-parameter curve-fitting with the experimental data using the following model function:

$$y(x) = \left(\frac{a}{x^3}\right)\exp\left[-\left(\frac{\ln\frac{x}{b}}{c}\right)^4\right]\Theta\left(b-x\right), \tag{3}$$

where $a \equiv \frac{I_0}{v_0} g_{inf} g_c^2$, $b \equiv g_{inf}$, and $c \equiv \frac{t_{cI}}{t_{cv}}$ are adjustable parameters. The fitted curves are superimposed on the GSD diagrams, and the revealed b and c parameter values are the following:

$$b_1 = 64.6\,nm, \quad c_1 = 1.42;$$

$$b_2 = 74.2\,nm, \quad c_2 = 1.38;$$

$$b_3 = 248\,nm, \quad c_2 = 0.53.$$

One of the main disadvantages of the used model is that it doesn't include the coalescence of grains. Therefore, the longer the droplet cools down (that is, the longer the grain growth and their subsequent merging takes), the poorer the resulting GSD is described by the **Equation 2**. This is exactly what is observed in the results in **Supplementary Fig. 9**: while for particles of 600 nm and 550 nm in size the fitting is rather successful, for larger particle (880 nm) the fitting attempt failed. Because the cooling rate is inversely proportional to the droplet diameter (see **Supplementary Note 6**).

Also, this model considers the crystallization only of a homogeneous melt, and not an eutectic mixture, as happens in our experiments. Still, since only Si crystallizes at first (see Main text), and initial atomic concentration of Au is fairly small (see **Supplementary Fig. 1**), we believe that this doesn't affect the quality side of the action and the KAMJ theory can be applied. At the same time, the presence of Au atoms during c-Si growth significantly limits the rate of this process (see Main text), which allows us to estimate v_0 as the interface velocity of Au content in the eutectic melt ($\sim$ 0,2 Å/ps).[6] This assumption makes it possible to calculate the characteristic nucleation and grain growth times (t_{cI} and t_{cv}) based on the results obtained during GSD fitting. The final values are:

$$t_{cI_1} = 4.6\,ns, \quad t_{cv_1} = 3.2\,ns;$$

$$t_{cI_2} = 5.1\,ns, \quad t_{cv_2} = 3.7\,ns;$$

$$t_{cI_3} = 6.6\,ns, \quad t_{cv_3} = 12.4\,ns.$$

Supplementary Note 6. On the cooling rate of liquid gold-silicon droplets

The main parameter that governs the solidification of liquid Au/Si droplets is the cooling rate of the system. Due to the low dimensions ($R \sim 0.5\mu m$) and sufficiently high thermal conductivity of the considered here gold-silicon bi-atomic solution ($\lambda_{Si} \approx 56\text{W/mK}$[11] and $\lambda_{Au} \approx 113\text{W/mK}$[12] at 1700 K), the temperature gradient inside the droplet can be neglected ($Bi \ll 1$, where Bi is the Biot number characterizing the heat transfer between the body and the environment). Therefore, the cooling rate K of the system can be written as follows:[4]

$$K = \frac{dT}{dt} = \frac{6h}{c_{pl}\rho d}(T - T_g) + \frac{6\varepsilon\sigma}{c_{pl}\rho d}(T^4 - T_w^4), \tag{4}$$

where the first term in the right part is responsible for the convection heat transfer, and the second one – for thermal radiation. T, T_g, and T_w are the droplet, surrounding media, and wall temperatures respectively; $c_p l$, ρ, h, and ε are the specific heat, density, convective heat transfer coefficient, and emissivity of the Au/Si melt; σ is Stefan Boltzmann constant.

Most importantly, the size of the droplet d is in the denominator of both terms, therefore the cooling rate is inversely proportional to this parameter. During the described solidification process, the cooling rate of the system (or, equivalently, the system size) plays a crucial role, as explored elsewhere.[7]

Supplementary Note 7. Finding the most appropriate k value during PL map clustering

As illustrated in **Supplementary Fig. 14**, the number of clusters (k) utilized to encode the data significantly influences the performance of the proposed authentication approach. When $k = 6$, the distributions of similarity indices (SI $= 1 -$ HD) for inter- and intra-device comparisons show a considerable overlap, leading to an increase in the false positive rate. Therefore, $k = 5$ was selected for our purposes as the largest integer at which reliable decisions can still be made. A similarity index threshold of 0.45 was set to help distinguish between different readings of the same PUF label and different PUF labels.

Supplementary Note 8. Estimating the encoding capacity of the second PUF protocol

In order to estimate the encoding capacity of our second PUF authentication protocol (which is based on computer-vision analysis of unique PL images), we used the well-established model proposed by Carro-Temboury et al.[13] According to this model, the encoding capacity can be expressed as follows:

$$EC = \left[C \left(1 + L \left(\frac{1}{\sqrt{D}} - 1 \right) \right)^2 + 1 \right]^{D\frac{R^2}{L^2}},$$

where C is number of possible responses for each image pixel after digitization, L is the length of each unit, D is the pattern filling density, and R is the effective image resolution ($R^2 = 500 \cdot 500 \cdot 0.35$ since 0.35 is the proportion of the Yin-Yang symbol to the entire 500x500 square image). For determining the exact values, we decided to binarize our images according to the gray scale intensity of each pixel (therefore $C = 2$). Specifically, the threshold intensity of 30 was chosen and the resulting binarized image is presented in **Supplementary Fig. 16c**. After such a procedure, the length of each unit and the pattern filling density were estimated to be 15 and 0.11, respectively. The estimated encoding capacity was then approximately 10^{141}.

Supplementary Note 9. On the number of possible different PL responses from one particle-based microstructure

As we stated in the main body of the manuscript, each laser-printed microstructure possesses not one but a number of unique PL spectra, depending on the location of the signal acquisition area and the polarization of the excitation wave. Indeed, each structure has dimensions of the order of 5×5 microns and consists of approximately 10 to 20 submicron particles (see **Supplementary Fig. 17a**), each exhibiting a distinct PL response. This feature stems from their unique internal organization, which also contributes to their strong polarization-dependent behavior.[14,15] Relative to the polarization of the incident laser pump, various plasmonic hot-spot modes can be excited inside the particle, which directly affects the field enhancement spectra inside its silicon grains. These changes, in turn, alter the Purcell factor values in the optical range, ultimately modifying the shape of the PL spectra (**Supplementary Fig. 17b**).

Aiming to maximize the number of distinct responses obtainable from a single structure while ensuring their uniqueness, we conducted a number of the following tests: First, we measured the PL maps from several randomly selected structures, varying the resolution from 2 by 2 (which corresponds to a single pixel size of 2.5 by 2.5 microns) to 10 by 10 (0.5 by 0.5 micron). Then we conducted a series of pairwise comparisons of spectra obtained from different parts of the resulting maps to make sure that they were distinguishable. As shown in **Supplementary Fig. 17c**, at a resolution of 4 by 4 or 5 by 5, almost all spectra turn out to be different, while at a resolution of 9 by 9, correlations between spectra measured from neighboring positions begin to appear, which is explained by the larger signal collection area compared to the cell size. Therefore, we chose a resolution of 5 by 5, which implies a single point size of 1 by 1 μm. Several matches not on the diagonal of the matrix can be attributed to a false positive result of the ML model used to compare our spectra. For all the measurements described here we utilized the high-aperture 100× objective with NA=0.75 (Mitutoyo M Plan APO NIR), which corresponds to the signal acquisition area

of approximately $1.3\mu m$ in diameter (at a wavelength of 800 nm). Also, to control the polarization of the incident laser beam, we used an achromatic half-wave plate (AHWP10M-980). Moreover, as we checked on **Supplementary Fig. 18**, the PL spectra measured under different excitation polarizations are deemed different in our authentication model (since the distance between their embeddings exceeds the cutoff threshold of 41.3, refer to the main body of the manuscript), which additionally confirms the viability of the proposed concept.

With all of the above, we can calculate that the number of unique spectral fingerprints that can be measured from one laser-printed structure is $N = 5 \times 5 \times 4 = 100$. Here, 5×5 is the number of possible signal acquisition positions, and 4 is responsible for the ability to change the polarization of incident light from 0° to 180° in 45-degree increments (as established for simplicity's sake).

It should be noted, though, that the arrangement of Au/Si particles within the microstructure is random and does not align with the grid's cell locations. Consequently, there may be some infrequent cells that have no particles inside and, as a result, yield weak PL signals. Fortunately, the presence of such cells will have a minor impact on the performance of the OTP token. If a weak-signal area is randomly selected during enrollment, it can be easily replaced with another location. Moreover, under sufficiently stable fabrication conditions, we anticipate that the fragmentation of the Au/Si bilayer film into hybrid particles will be uniform, resulting in a high density of particles distributed evenly throughout the microstructure (see **Supplementary Fig. 2**). Therefore, the occurrence of weak-signal cells will be relatively rare.

Supplementary Note 10. On the concept of One-Time Password verification

One-time password (OTP) verification using an OTP token is a cornerstone security mechanism designed to authenticate users during various online/offline operations. In the most secure implementations, an OTP token is typically a physical device that stores or generates unique responses depending on the specified request, and only the verification server can predict beforehand these responses. When a user tries to access a secure system, they must first enter their username and password, followed by the OTP generated by the token in response to a specific, never repeated server request. This OTP response is valid for only a short duration of time, which provides an additional security. Consequently, even if a user's personal data are compromised, unauthorized access is prevented without immediate possession of an OTP token. This method improves security by requiring both something the user knows (their password) and something they possess (the OTP token), which significantly increases the difficulty for possible attackers.

In general, any OTP verification token should embody a system that securely stores (or unpredictably generates) a substantial number of genuinely random keys. These keys must remain confidential until used, never be reused, and be completely independent of each other.[16] Additionally, in order to ensure perfect protection, it is necessary to ensure that it is almost impossible to gain full access to all the keys stored in the token (as we describe in the main body of our work). While such OTP systems have been widely recognized in industry, their practical electronic implementations face a number of limitations in modern cryptographic applications.[16–18] The primary challenge hindering the widespread adoption of OTP schemes lies in the potential vulnerability of electronic hardware to physical attacks, such as discrete reset,[19] imaging,[20] and freezing[21] techniques, which can compromise partial or complete verification keys. Additionally, it is necessary to provide the generation and secure storage of a huge number of truly random and uncorrelated keys. Therefore, there is a growing quest for novel implementations of the OTP concept, for example, using optical methods.[16–18]

At this standpoint, the all-optical OTP verification token proposed in our work offers several notable advantages. First, the optical readout method employed enables the acquisition of high-entropy keys that are stored on the nanoscale with remarkably high storage density (see **Supplementary Note 16**). Second, as we demonstrated in the **Supplementary Note 12**, the likelihood of a third party being able to randomly access the key required for verification approaches zero, which underscores the confidentiality of the proposed scheme. Finally, our model holds significant promise for the future cryptographic implementations in the upcoming era of photonic computing and optical communications.[22–24]

Supplementary Note 11. Comparing the production and full readout times for the OTP verification token concept

In our laser-printing experiments, operating at a beam movement speed of 50 μm per second enables high-throughput fabrication of microstructures at a rate of roughly 200 units per minute. Employing the laser beam multiplexing technique can further boost this rate by two orders of magnitude, reaching up to 20,000 units per minute.[25–27] Considering that each generated microstructure yields 100 unique fingerprints (as demonstrated in **Supplementary Note 9**), we estimate a production capacity of 2 million random keys per minute of continuous laser printing.

Before calculating the time required to measure all generated keys, it is worth noting that it depends heavily on the excitation laser's fluence. For example, setting the laser's irradiation power density to ~ 4 mJ/cm^2 (as we did for our first concept of anticounterfeiting label) makes it possible to measure the PL signal in less than 0,2 seconds. However, reducing the laser fluence increases the measurement time needed to acquire a high-quality, low-noise spectrum. Furthermore, the signal shape strongly depends on the laser fluence due to PL nonlinearity, which is characterized by a complex and unpredictable wavelength-dependent slope (see **Fig. 2c** in the main part of the manuscript). Therefore, if the manufacturer, who enrolls the fabricated sample, uses low laser intensities with a relatively high readout time, then all subsequent measurements by users should be performed in the same way. For our OTP token scheme, we set laser fluence to $\sim 1{,}5$ mJ/cm^2, providing a characteristic readout time of roughly 3 seconds. In this scenario, only 20 spectra can be measured per minute (if we don't account for the time needed for accurate acquisition area positioning).

Ultimately, we can confirm that the time required to fabricate an array of Au/Si microstructures is remarkably efficient compared to the time needed for its complete readout. The estimated ratio stands at 1:100,000, signifying a five-orders-of-magnitude difference.

Supplementary Note 12. The impact of the number of spectra comparisons during verification on the OTP token's performance

For simplicity, in the main part of this manuscript, we described the token verification process, in which the decision was made based on a comparison of **one** pair of spectra. The first spectrum was measured and sent by the user, and the second one was stored in the database. However, to improve the degree of token protection, it is necessary to increase the number of such comparisons. In the general case, upon a user's request, the server provides the coordinates (including the required laser polarizations) of $2n$ points. The spectra measured from n of them are contained in the database, and the other n has never been measured before (they are chosen randomly). After the user's submission, the server makes the validation decision during the sequential comparison of n pairs of spectra.

The greater the specific value of n, the greater the verdict accuracy. Furthermore, the token's service life grows. By the term *service time*, we mean the period during which it is possible to state, with a given accuracy, that the token has not been compromised. An obvious upper estimate of service time is the time required to fully measure all possible token keys. Indeed, if one user possessed the token for a longer duration than the service time, they could record all the spectra from it and therefore have the opportunity to undergo verification without actually needing the token. (Recall that, thanks to the dynamic nature of the token database, it is always necessary to have the token physically present in order to undergo verification. This is one of the key features of the developed concept.) So, the longer the token was stored by one person, the more likely it is that they managed to measure the spectra that will be needed to complete the next verification cycle. We estimate such a probability by introducing the following formula:

$$P = \left(\frac{\eta t}{N}\right)^n,$$

where P is the probability of accidentally measuring the n spectra required for the future verification cycle as a result of continuous key measurement at a rate of η[spectra/min] during

time t[min] (a.k.a. the risk score). $N = H * T$ is the number of all keys concealed inside the token fabricated for time T[min] at a speed rate of H[keys/min]. As an illustration, suppose that $T = 60$ min, $H = 2 \cdot 10^6$ keys per minute (so $N = 1{,}2 \cdot 10^8$), and the spectra measuring rate is 20 spectra per minute (see **Supplementary Note 11**). If we set the treshold for risk score to 0.01, then the token's service time will be about 42 days for $n = 1$ and almost 7 years for $n = 9$ (see **Supplementary Fig. 19a,b**).

As for the accuracy of multiple spectra comparison, we assess it in the following form:

$$\mathrm{Acc}_N = \sum_{k=0}^{\lfloor \frac{n-1}{2} \rfloor} p^{n-k} \left(1-p\right)^k C_n^k,$$

where $p = 1 - \mathrm{Acc}_1$ is the probability of an error in one comparison. For our trained ML model $\mathrm{Acc}_1 = 0{,}97$ and $p = 0{,}03$ (see **Supplementary Fig. 25**). Therefore, if we use, for example, 5 comparisons of spectra to complete verification, then the decision's error rate will be about $3 \cdot 10^{-4}$ (**Supplementary Fig. 19c**).

If we assume that the manufacturer will spend about an hour enrolling the token and creating a database, we can estimate its volume at 1200 spectra. Then, if we disclose the location of five spectra in one verification cycle, the entire database will be enough for 240 cycles. This can be quite sufficient, depending on the specific application of the token. If the database is depleted, the token can be sent back to the manufacturer (or any other trusted party) to update it. Also, it is useful to note that in the scenario used for calculations ($T = 60$ min, $H = 2 \cdot 10^6$ keys per minute), the physical size of the token will be on the order of 1 by 1 mm^2 which is quite miniature.

Supplementary Note 13. NIST testing of ML-generated embeddings

To assess the randomness of the embedding keys generated by our trained ML model for each PL spectrum, we employed a widely recognized NIST testing procedure.[28,29] We randomly selected 400 distinct embeddings from our database and subjected them to a series of randomness tests from the NIST test suite. It is important to note that, due to the continuous distribution of our key values (**Supplementary Fig. 21**), we binarized them by comparing each embedding coordinate's value to its average. The results are presented in **Table 2**.

Supplementary Note 14. Calculating information entropy of ML-generated embeddings

In addition to NIST testing, we calculated the information entropy for our ML-generated embeddings. According to the third proposed PUF-based protocol, our trained ML model transforms an input PL spectrum into a 1024-dimensional embedding vector that serves as a unique unclonable key. As demonstrated in **Supplementary Fig. 21**, the coordinates of these vectors are continuously distributed and exhibit a Gaussian-like bell shape. To quantify their distribution, we computed the continuous entropy (or differential entropy[30]) for each of the 1024 embedding dimensions using a database of 2148 different embeddings. Our results are presented in **Supplementary Fig. 20**. The mean value of entropy, which is carried by each embedding coordinate, is approximately 7.3 (with a variance of around 4.3), indicating a very high level of unique information saturation. Additionally, we present the results of a more conventional discrete entropy calculation.[30] For this, we binarized the embedding coordinate values based on their deviation from the mean value for each specific coordinate. The mean entropy value obtained is 0.97, with a variance of 0.0009, which implies a uniform level of bit complexity and their complete unpredictability.

Supplementary Note 15. On the encoding capacity of embedding space

To calculate the encoding capacity (EC) of the embedding space, we can place points into the N-dimensional embedding space such that the distance between them is greater than or equal to the cutoff distance (CD). As we got in our calculations, in the embedding space, the coordinates range from $-l$ to l ($l = 6$, see **Supplementary Fig. 21**). The exact solution to this problem in high dimensions is quite challenging, as it is equivalent to the problem of close sphere packing. However, we can estimate the lower bound of EC by making each coordinate of the point either $-l$ or l. A point's position in that case can be represented by a bit string of length N: $(a_i)_{i=0}^{N}$, $a_i \in \mathbb{Z}_2$, $x_i = l \cdot (2a_i - 1)$. The distance between points is equal to

$$d_p((a_i), (b_i)) = \sqrt{\sum_{i=1}^{N} (a_i - b_i)^2 \cdot (2l)^2} = 2l\sqrt{d((a_i), (b_i))},$$

where d is the Hamming distance between the bit strings. Our requirement is for each distance between points to be greater than CD translates to $2l\sqrt{d} \geq CD$, which means $d \geq \left(\frac{CD}{2l}\right)^2$. We can estimate the lower bound of the number of points in $(\mathbb{Z}_2)^N$ with distance $d \geq d_0 = \left\lceil \left(\frac{CD}{2l}\right)^2 \right\rceil$ by using the Gilbert–Varshamov bound.[31,32] With $CD \approx 41.3$, which was set during the model adjustment, we obtain that

$$EC \geq n_{points} \geq n_{min} = \frac{2^n}{\sum_{k=0}^{d_0-1} \binom{n}{k} (2-1)^k} \geq 10^{280}.$$

Notably, such a considerable encoding capacity achieved implies that the effective amount of information contained in each embedded vector is about 930 bits (since $10^{280} \approx 2^{930}$). Considering that in our OTP token model, each 1 by 1 μm^2 area contains four unique PL spectra (see **Supplementary Note 9**), we can estimate the density of information recording as $930 \cdot 4 = 3720$ bits per square micron. In generally accepted units of measurement, this is equivalent to 54 gigabits per square inch, which turns out to be higher than the corresponding values of commercially available optical discs and even some magnetic disk technologies.[33,34]

Supplementary Note 16. On the concept and calculation of storage density

When discussing efforts to reduce the critical sizes of PUFs, an essential metric for evaluating system performance is the storage density. This metric quantifies the amount of unique information extracted per unit area of a PUF label. The lower the PUF's critical sizes *and* the higher the entropy of the measured PUF responses, the greater the storage density value will be. It can be argued that this parameter provides a more in-depth understanding of PUF performance than traditional metrics such as encoding capacity.[35,36]

Within the concept of storage density, we believe that the broadband photoluminescence of our hybrid Au/Si particles is particularly advantageous, as it encodes a significant amount of information about the internal structure of these particles. To illustrate this point, we have compiled a comparative table that highlights the storage density values from recent related works (see **Supplementary Table 3**). Below, we present our calculations of the storage density for all three proposed PUF concepts.

1) The first PUF label model proposed, which is based on PL mapping and spectral decomposition, utilizes a 10x10 mapping grid with a pixel step size of approximately 14 micrometers. Consequently, each pixel covers an area of 196 μm^2, allowing us to capture an integrated PL signal from many laser-printed microstructures and numerous Au/Si particles. Such a relatively coarse mapping resolution was intentionally selected to minimize total measurement time and reduce the costs associated with the required measurement equipment. After conducting spectral decomposition and applying the clustering procedure with k=5 (as detailed in the **Methods** section), we find that each pixel in the map encodes five quinary numbers, which corresponds to $5 \cdot \log_2(5) \approx 12$ bits. However, because of the correlations present among these values, the effective bit size of such a set of numbers is approximately 0.346 (see **Methods**). Consequently, each 14x14 μm^2 area stores around $5 \cdot \log_2(5) \cdot 0.346 \approx 4$ bits of unique information. This results in an effective storage density of $4/196 = 0{,}02$ bit per square micrometer. Please note that if choosing a more precise mapping resolution (for example, with the step of 1 μm), the storage density will increase up to 4 bit/μm^2.

2) The second PUF label model employs direct PL imaging of laser-printed microstructures captured with a standard digital camera. The algorithm developed for this model compares pairs of PL images to determine whether they originate from the same label. It focuses on the brightest and clearest areas of the images (features) that have characteristic sizes of approximately 2-3 micrometers. The total area of a single laser-printed Yin-Yang pattern is about 5000 μm^2. The encoding capacity of this system was estimated to be approximately 10^{141} (see **Supplementary Note 8**) which effectively corresponds to $\log_2(10^{141}) = 468$ unique bits and an effective storage density of $468/5000 = 0.09$ bit/μm^2.

3) Our final and most beneficial PUF concept is based on encoding individual PL spectra using machine-learning approach. After fine-tuning our ML model, we achieved an encoding capacity of 10^{280} (**Supplementary Note 15**), which is equivalent to $\log_2(10^{280}) = 930$ bits of unique information. In the developed protocol, the PL responses are measured from areas as small as 1 μm^2 under laser excitations with four different incident polarizations. This results in an effective storage density of $4 \cdot 930/1 = 3720$ bit/μm^2.

Supplementary Note 17. Calculation of the overall cost of a single PUF label

Here, we provide the mildest estimation of the costs associated with (a) fabricating and (b) reading a single PUF label.

(a) Fabrication costs

Due to the considerably high costs associated with the equipment required for fs-laser fabrication of our PUFs, the contribution of material costs (which we estimate to be as low as 10^{-4} USD per PUF) appears to be almost negligible. Below, we list the primary laboratory machines utilized in our experiments, which represent the largest portion of the overall fabrication expenses (all the presented values are approximate):

1) Magnetron sputtering machine (BockEdwards Auto 500), 10 k$

2) Plasma-enhanced chemical vapor deposition machine (Oxford Instruments Plasmalab System 100), $200k$$

3) Ti:Sapphire fs-laser (TiF-100 F, Avesta Project), 100 k$

4) Air-bearing 3D positioning system (ABL1000, Aerotech), 200 k$

5) Optical table + Lenses + Optomechanics, 20 k$

In total: $\sim$ 530 k$.

This equipment can be reliably used over a period of at least 10 years. Assuming 300 days of laser-writing work per year, we estimate that about $2 \cdot 10^5$ PUF labels (laser-printed QR codes or Ying-Yang drawings, as we shown in the main body of the work) can be produced annualy (with a production rate of 30 labels per hour). Consequently, the average fabrication cost for each PUF label is less than 0,3 US dollars. If we consider the fabrication of our PUF-enabled token, which offers much more practical value and security possibilities than a standard PUF label, the production time increases to 1 hour per sample (see **Supplementary Note 11**). As a result, the average fabrication cost for each PUF-enabled token is estimated to be around 8-9 US dollars. Please note that when using existing industrial scalable equipment rather than our laboratory setup (and if depositing silicon film by magnetron sputtering instead of the PECVD technique), the total fabrication costs may

drop drastically by almost one order of magnitude.

Ultimately, the prices obtained are of the same order of magnitude as some of the analogues proposed in the literature.[37] Given the high degree of protection provided by our *nanoscale-enabled* PUFs, we believe that they can find their niche for industrial use.

(b) PUF readout costs

The list of the major parts of a setup that we used to measure PL response from our PUF labels is the following (all the presented values are approximate):

1) Yb^{3+} fs-laser system (TeMa, Avesta Project), 50 k$

2) Fiber-optic spectrometer (Avantes), 5 k$ (Although in our work we utilized a laboratory Horiba LabRam HR spectrometer valued at 100 k$, we also demonstrated the feasibility of using a less expensive industrial spectrometer, see **Supplementary Note 18**);

3) Three-axis piezostage (AIST Project), 5 k$;

4) Optical table + Lenses + Optomechanics, 20 k$;

In total: $\sim$ 80 k$.

If we were to replace our specialized laboratory fs-laser and other optomechanical components with industrial fiber-optic equivalents, the total cost could be reduced to approximately 20 k$. We recognize that the resulting costs are substantial, which restricts the range of potential applications. However, our primary motivation for utilizing our spectral PUFs is to provide the highest level of protection over the long term (decades). This is especially crucial in an upcoming era when conventional PUFs, characterized by microscale spatial randomness, will become vulnerable due to advancements in precise micro-manipulation techniques.

Supplementary Note 18. PL measurements with an industrial optical fiber spectrometer

To explore potential simplifications in the readout system, we conducted additional experiments using a standard, less sensitive optical fiber spectrometer (Avantes AvaSpec-2048). As shown in **Supplementary Fig. 22**, this industrial spectrometer delivered robust results, achieving efficient PL spectrum measurements with a 1-second acquisition time. It is important to emphasize, though, that obtaining consistent PL spectra, regardless of the type of spectrometer used, requires careful consideration of the spectrometer's quantum efficiency and other critical parameters, such as spectral resolution. These parameters are typically calibrated and certified for most laboratory and industrial equipment.

Supplementary Note 19. On the environmental stability of proposed PL-based PUFs

Gold (a noble metal) and silicon (the most common semiconductor) were chosen as the foundation for spectral PUF labels due to their desirable properties. Beyond their exceptional chemical and photo-stability, these materials offer high thermal and aging resistance. Indeed, it is known that Au/Si systems demonstrate no structural changes below 130°C and possess a virtually unlimited lifespan under normal conditions.[38]

To improve the mechanical stability of the created samples, we encapsulated them by spin-coating (1000 rpm, 30 s) polydimethylsiloxane (PDMS). The applied PDMS layer with a thickness of about 300–500 microns had practically no negative effect on the measured PL signal due to its transparency in the visible and near-infrared ranges (see **Supplementary Fig. 23**).

Additionally, we have investigated the stability of our samples under various environmental conditions. To control whether the label response has changed or not, we calculated the distance between embeddings (vectors) generated by our ML model for a pair of spectra measured before and after a certain stability experiment. If the obtained value is lower than the cutoff threshold (< 41.3, see **Supplementary Note 15** or the main body of the manuscript), then our PUFs are stable with respect to the corresponding environmental disturbance.

Time stability

First, to investigate long-term stability, we have compared the PL spectra of the same Au/Si structures before and after two years of storage under laboratory conditions. These spectra are shown in **Supplementary Fig. 24a**. The distance calculated between the ML-generated embeddings for them is 13.82, which is less than the threshold of 41.3, indicating strong ageing resistance.

Humidity and Sunlight Stability

We addressed another concern about the stability of our samples in a humid environment or

under sunlight exposure, keeping them outside (in open air) for two hours during the daytime in our hometown of St. Petersburg. On the cloudless day of the experiment, the average humidity was 93% and the temperature was around 3℃. As a result, our PUFs performed well, thanks to the exceptional photostability of materials used as well as protective polymer coating (**Supplementary Fig. 24b**).

Continuous laser excitation/measurements

To confirm the durability of our structures against laser irradiation and to demonstrate the ability of repeatedly measuring their signal, we monitored the stability of PL spectra for a one-hour period of continuous measurements. The **Supplementary Fig. 24c** shows great consistency in the obtained results. The distances corresponding to the measured spectra varied in the range of 7.65-15.06, which is much less than the validation threshold.

Low temperatures

We also tested the effect of low temperatures on the stability of the PL signal of our hybrid particles. To do this, we stored our samples in a freeze dryer at -19℃ for one hour. The PL spectra measured before and after this experiment are shown in **Supplementary Fig. 24d**. The distance calculated between the ML-generated embeddings for these spectra was 20, which indicates that low temperatures did not affect our PUFs.

Elevated temperature during PL measurements

It was also important to ensure that temperature variations directly during PL measurements do not affect the resulting spectra. To this end, we heated our PUF labels using a thermoelectric module TB-65-0.6-0.8 with a QJ1803C power supply. We started at room temperature and increased it up to 50℃ while simultaneously recording the PL spectra (**Supplementary Fig. 24e**). This experiment also turned out to be successful.

High temperatures

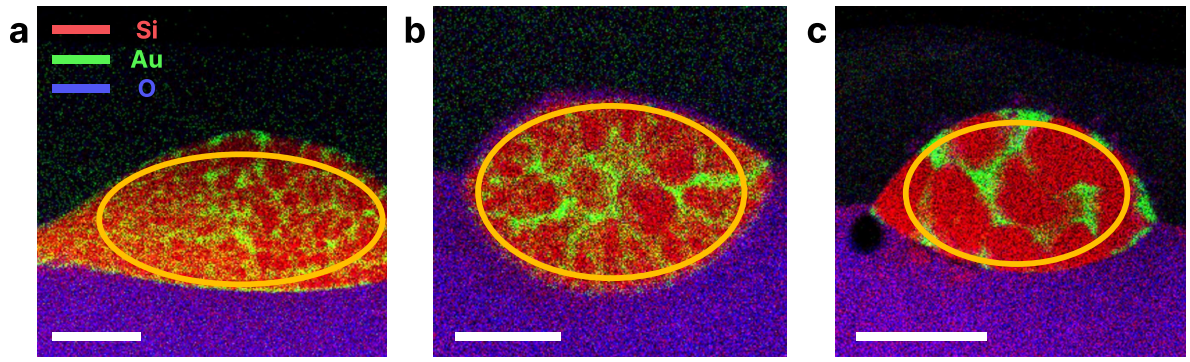
We also investigated the influence of high temperatures on the PL signal of our Au/Si particles. For this, we heated our samples to temperatures of 50-200℃ for 10 minutes using the hotplate function of the MR Hei-Tec setup (Heidolph). The PL spectra measured be-

fore and after a heating to a certain temperature are presented in **Supplementary Fig. 24f**. Additionally, **Supplementary Fig. 24j** shows the temperature dependence of the distance calculated between the ML-generated embeddings for the initial and modified (or non-modified) spectra. These results showcase that our samples remain stable under temperatures of as high as 110℃.

Mechanical abrasion

We tested the stability of our PDMS-coated samples by subjecting them to various mechanical stresses, such as friction with granulated sugar and flow of deionized water (see **Supplementary Fig. 24h,i** and **Supplementary Movie 1**). After these tests, we did not observe any changes in the appearance of the sample or in the form of measured PL spectra (**Supplementary Fig. 24g**). Therefore, we concluded that our samples are stable under mechanical abrasion.

To sum up, as we have checked, our samples have demonstrated solid results in terms of environmental stability. While we can't say that we have achieved outperforming temperature or mechanical stability (there are extremely stable PUF concepts proposed in the literature, see[37,39,40]), we do believe there is great potential for our labels to be used for highly reliable protection of valuable goods or identities.

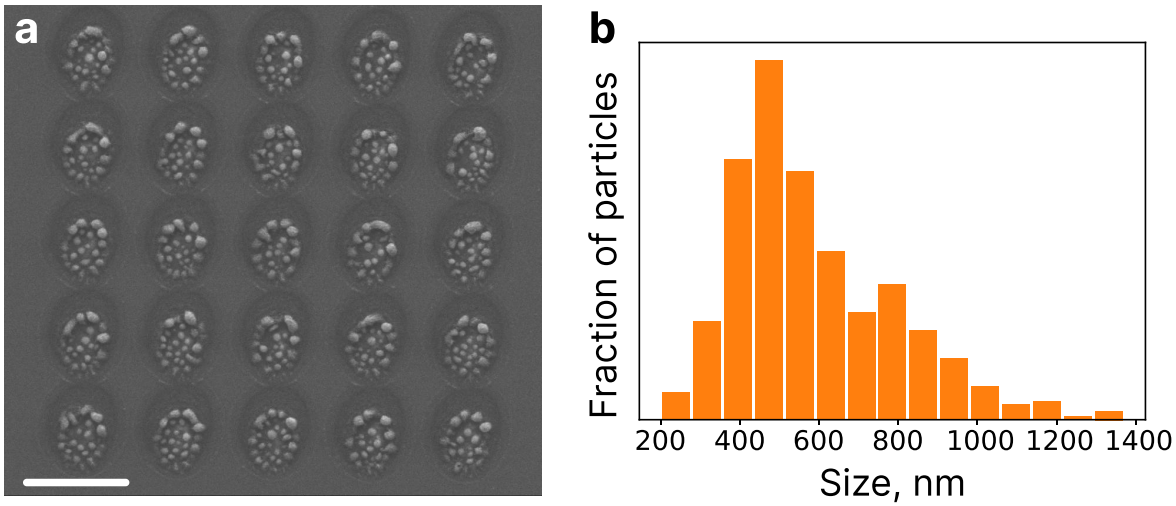


Element	Atom%
O	3
Si	91
Au	6

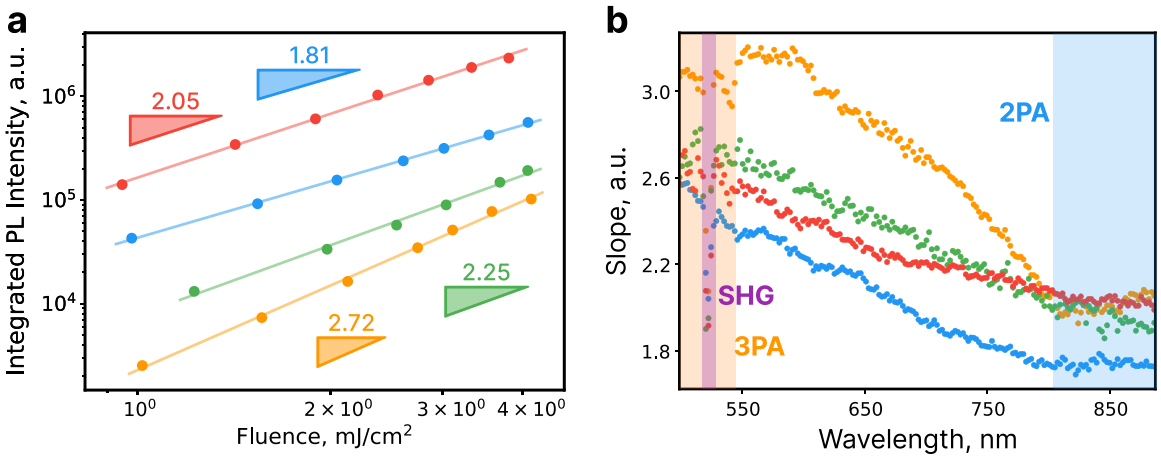
Element	Atom%
O	5
Si	85
Au	9

Element	Atom%
O	8
Si	82
Au	10

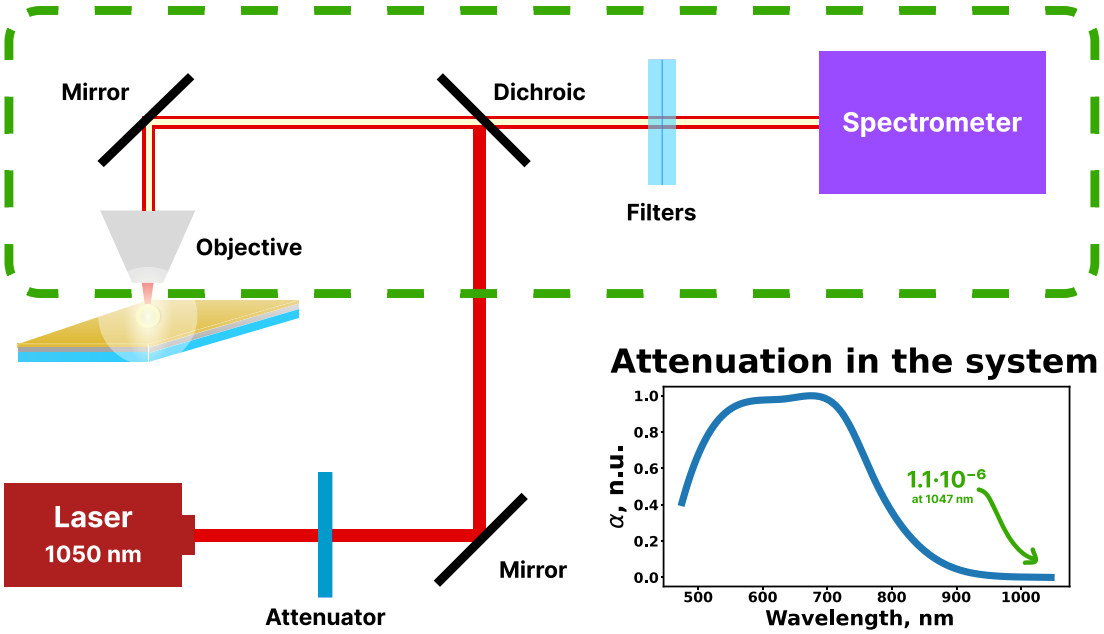
Supplementary Figure 1: **Energy-dispersive X-ray spectroscopy (EDS) maps of cross sections of three investigated Au/Si particles.** Scale bars are **(a-b)** 200 nm and **(c)** 500 nm. Tables below reveal the atomic concentrations of Si, Au, and O atoms inside highlighted areas.



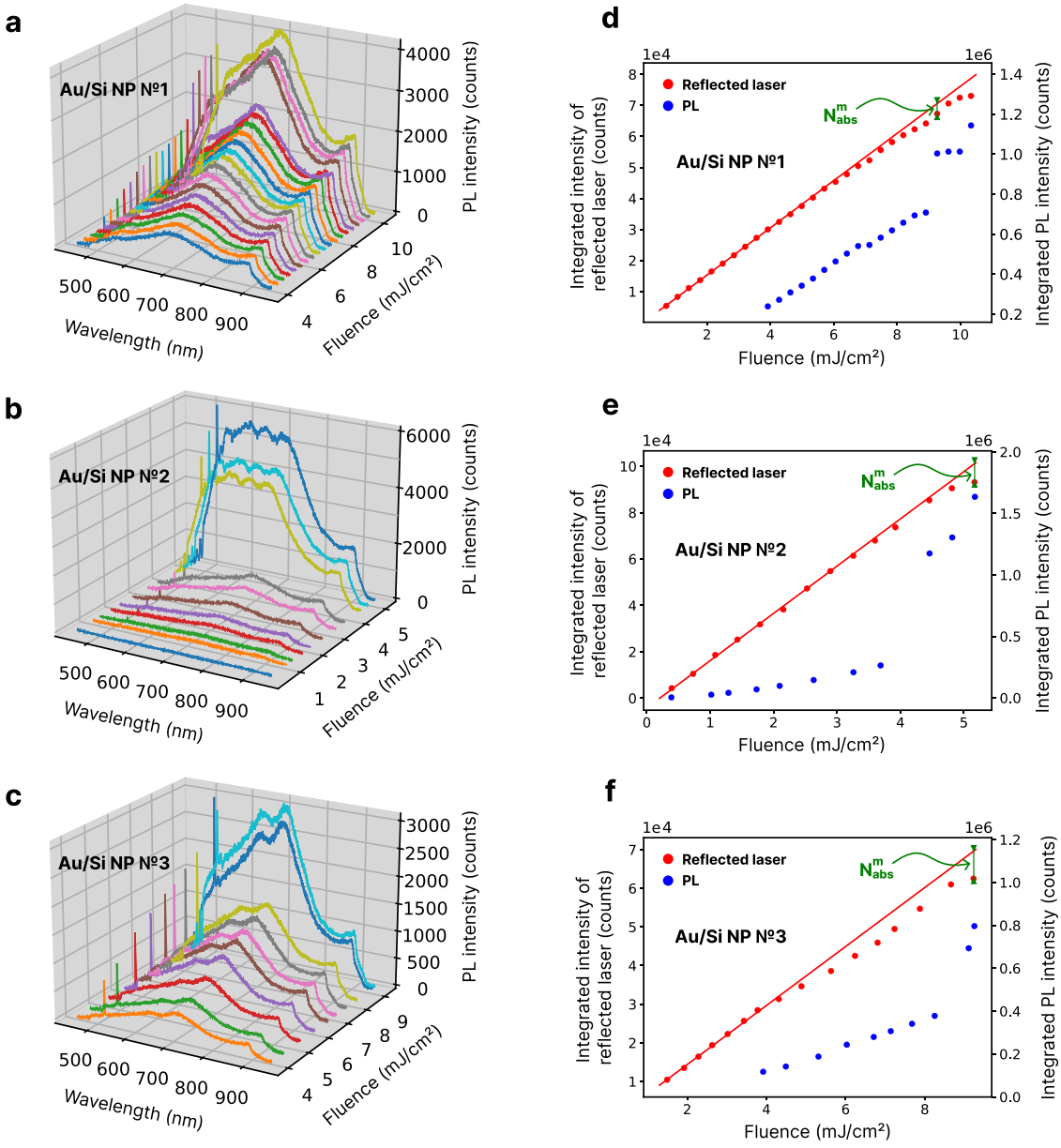
Supplementary Figure 2: **Size distribution of laser-fabricated hybrid Au/Si particles. (a)** The Scanning Electron Microscopy (SEM) image of an 5×5 array of laser-printed particle-based microstructures (Scale bar is 7 μm). **(b)** The size distribution of hybrid Au/Si particles in these structures.



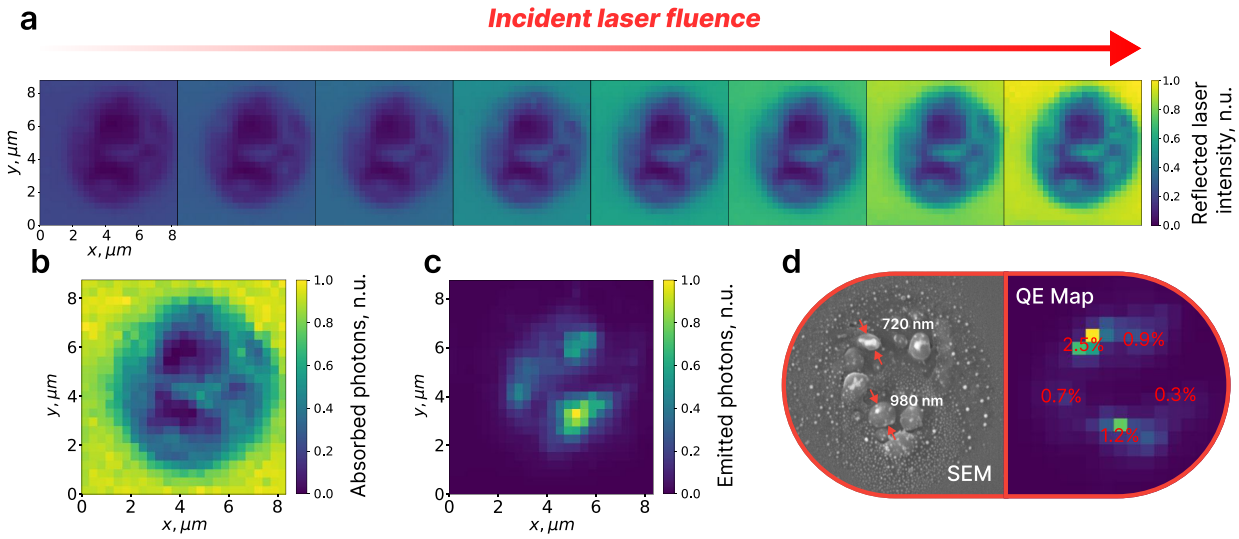
Supplementary Figure 3: **Au/Si Photoluminescence Slopes.** **(a)** The PL slopes of four randomly chosen Au/Si particles and **(b)** their dependence on wavelength.



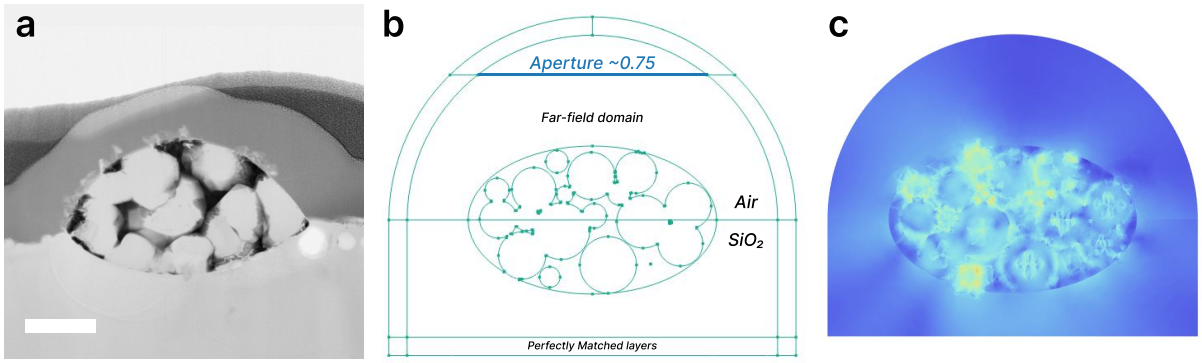
Supplementary Figure 4: The scheme of the setup used to estimate quantum efficiency of hybrid Au/Si nanoparticles. The graph displays the calculated dependence of the relative attenuation coefficient on the wavelength in the experimental system.



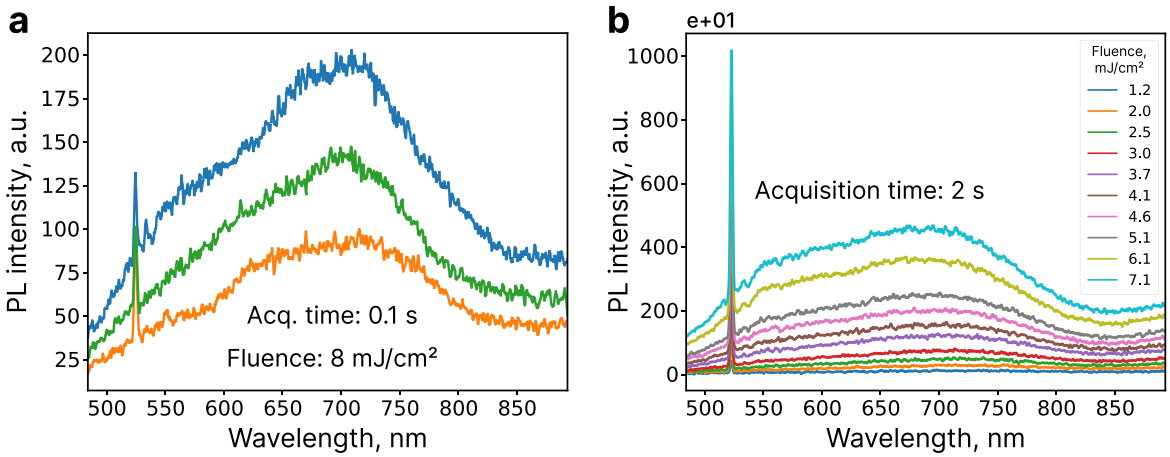
Supplementary Figure 5: **Quantum efficiency estimations.** The investigation of white-light signal **(a–c)** and reflected laser intensity **(d–f)** dependencies on the excitation laser fluence for three different hybrid Au/Si particles. The red lines on graphs **d–f** indicate the extrapolation of linear relationship between the integrated intensity of the reflected laser and the excitation power density. The green arrows correspond to the estimated number of photons absorbed by the Au/Si NP.



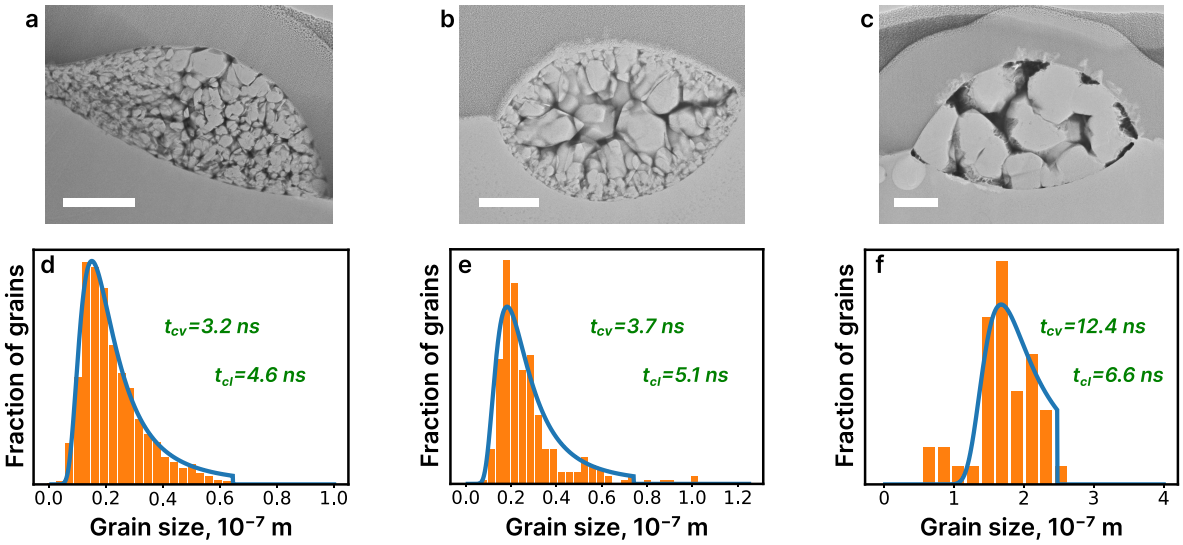
Supplementary Figure 6: **Quantum efficiency mapping.** **(a)** Maps of the reflected laser intensity at different incident fluences (2–8 mJ/cm^2). Estimated numbers of absorbed **(b)** and emitted **(c)** photons at excitation laser fluence of 8 mJ/cm^2. **(d)** Resulting QE map and SEM image of the corresponding structure.



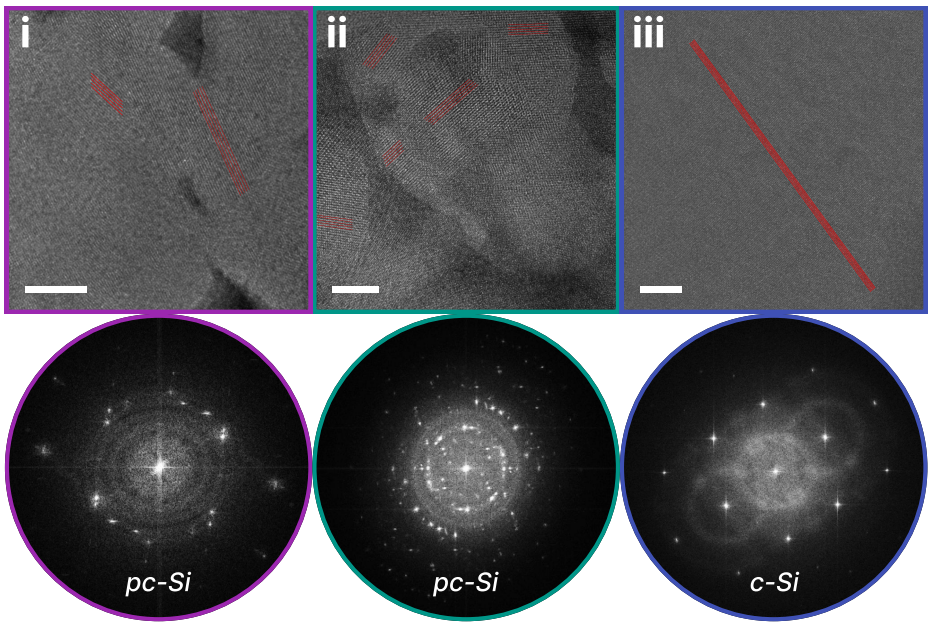
Supplementary Figure 7: **Simulation of the PL radiation pattern of hybrid Au/Si particles.** **(a)** Cross section STEM view of one of the investigated particles (scale bar is 300 um) and **(b)** cross section view of the corresponding COMSOL model. **(c)** Field distribution in the model under the radiation of ∼1000 coherent electric dipole emitters randomly distributed inside the *c*-Si grains in the particle. Radiation wavelength is 650 nm.



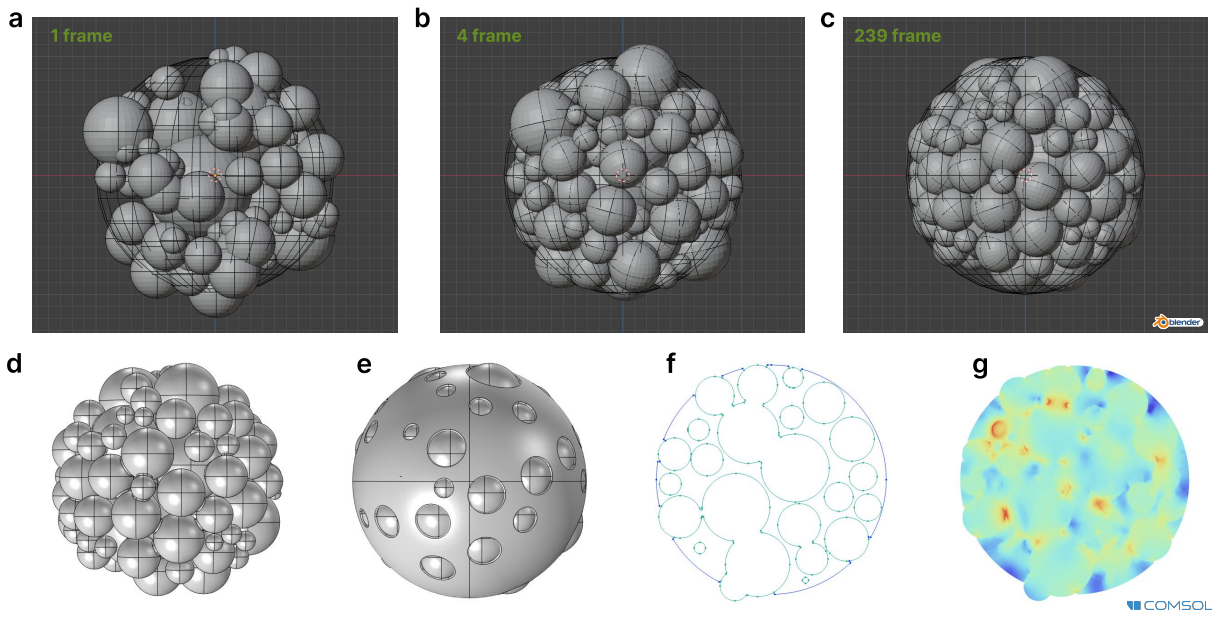
Supplementary Figure 8: **On the acquisition times necessary for obtaining low-noise PL spectra. (a)** The PL spectra of three randomly chosen Au/Si particles measured with the acquisition time of 0,1 seconds and the pump laser fluence of $\sim$ 8 mJ/cm^2. **(b)** The dependence of PL spectra measured with the acquisition time of 2 seconds on the pump laser fluence.



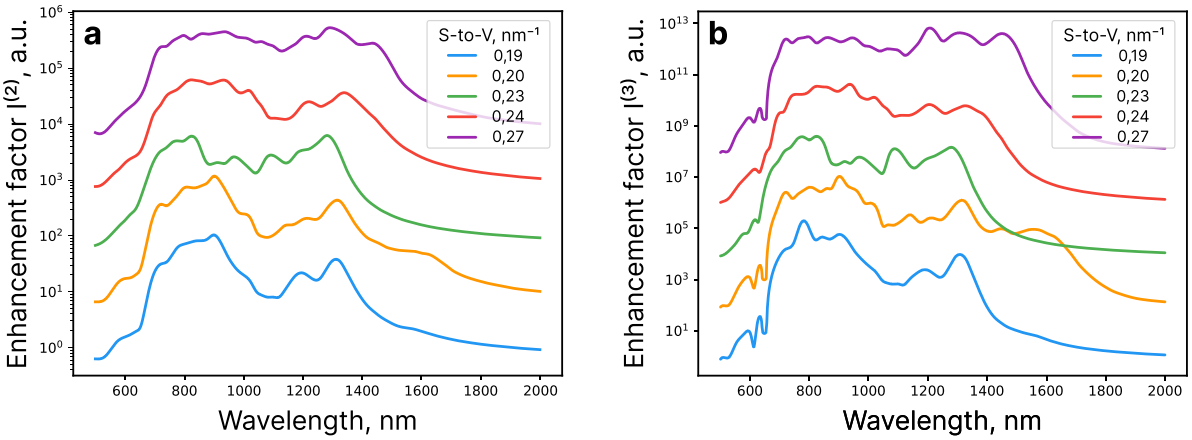
Supplementary Figure 9: **Grain size distribution characterization for three different Au/Si particles. (a-c)** The cross-sectional STEM views of the investigated particles (scale bars are 200 nm) and **(d-f)** the corresponding grain size distributions retrieved from these images. Curve fitting was carried out using KAMJ model according to the **Equation 3**. The inserts on the diagrams provide the estimated grain growth and nucleation times retrieved thanks to the fitting and a number of assumptions described in the text.



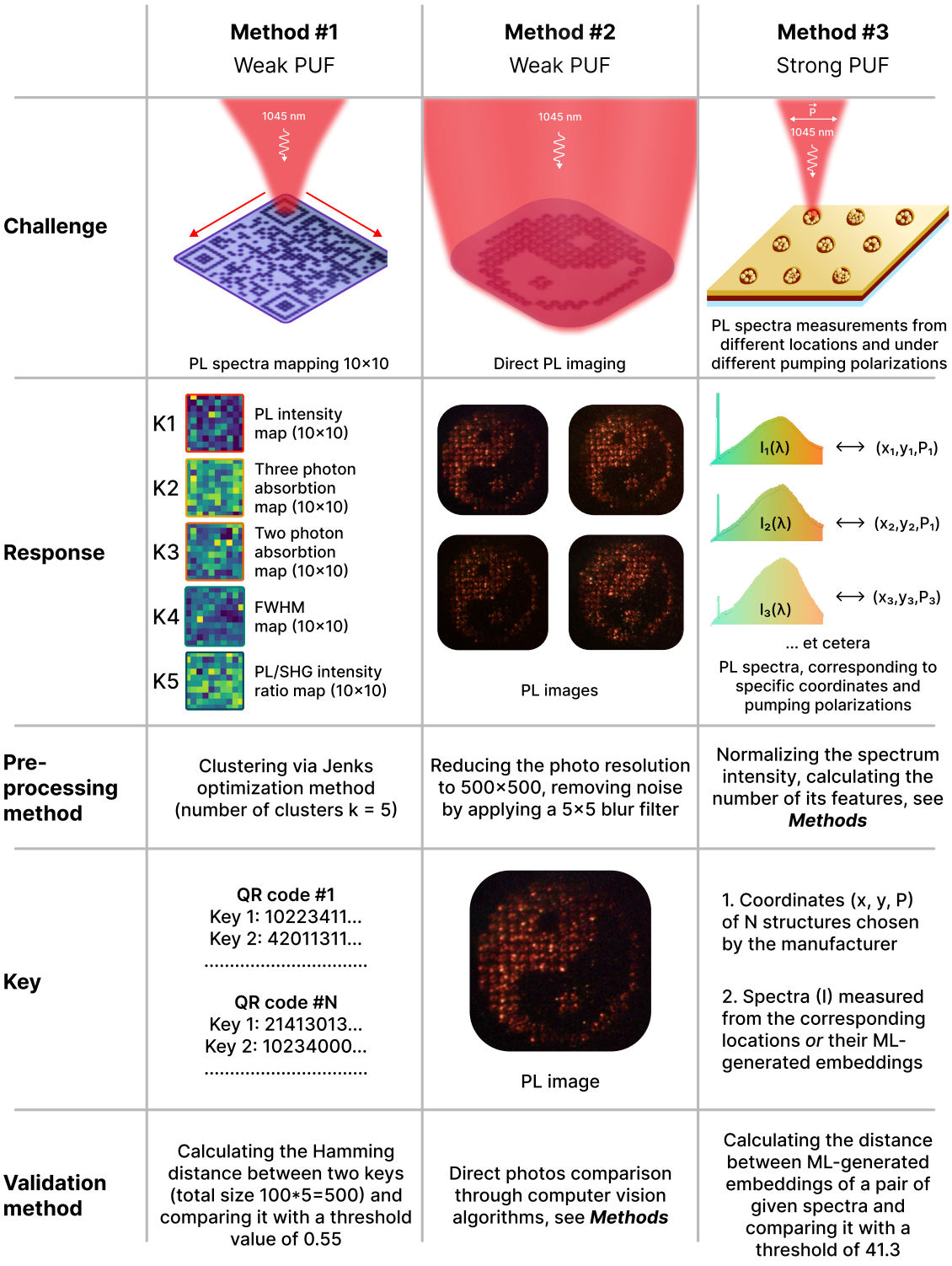
Supplementary Figure 10: **High-resolution transmission electron microscopy (HRTEM) images of selected areas of silicon grains in the investigated Au/Si particles and their fast Fourier transform (FFT) analysis.** The numbering **(i-iii)** correspond to the one set out those in the **Fig. 3** in the main part of this work. Based on the FFT HRTEM analyses, it can be concluded that silicon is predominantly in a polycrystalline phase. Some crystalline areas are indicated by parallel red lines for illustrative purposes.



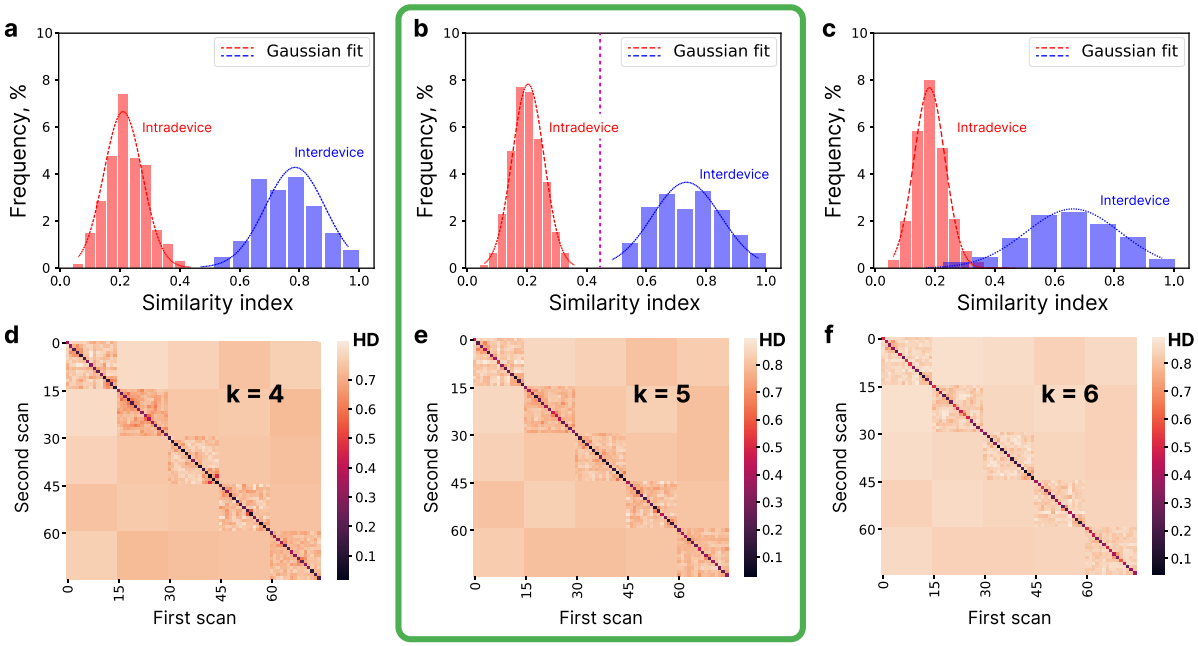
Supplementary Figure 11: **An example of step-by-step generation of the particle interior geometry in Blender and its post-processing in COMSOL Multiphysics.** **(a-c)** Creating randomly arranged spheres of specified sizes inside a larger spherical volume and running the rigid body simulation in Blender. **(d-e)** Generating spheres in COMSOL with locations and sizes retrieved from the Blender simulation and subtracting the obtained geometry (corresponding to the *c*-Si grains) from the larger sphere (corresponding to the gold volume). Filleting all the intersections in the model. **(f)** The cross section view of the obtained geometry and **(g)** corresponding field distribution inside the particle under plane wave illumination (logarithmic scale).



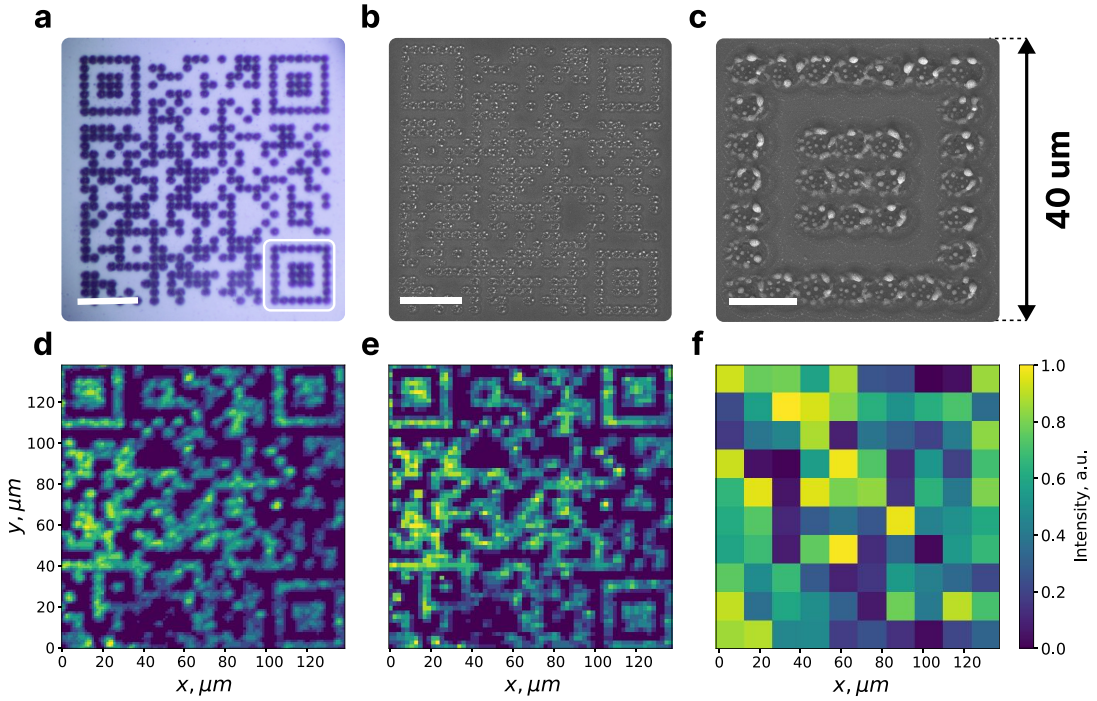
Supplementary Figure 12: **Some of the results of numerical simulations of the field enhancement factor (EF) range for different Au/Si particle models.** EF was calculated in two ways: as a square **(a)** or cube **(b)** of the relative field intensity. The plot legends include information about the simulated particles' S-to-V values. It is clearly seen that increasing the surface-to-volume ratio extends the EF range while retaining almost similar maximum values. Notably, the broadening occurs on both the blue and red sides, with a preference for the red side.



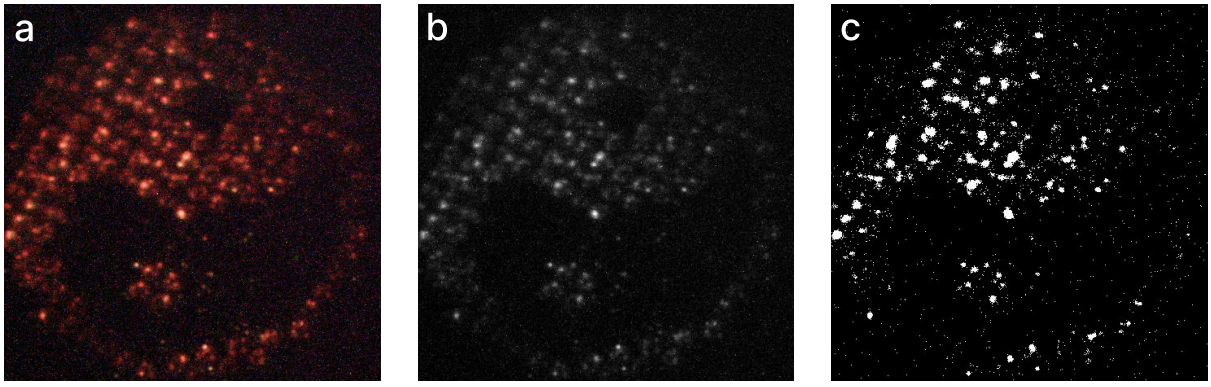
Supplementary Figure 13: A scheme summarizing the Challenge, Response, Post-processing method, Key, and Validation method for each of the three proposed PUF protocols



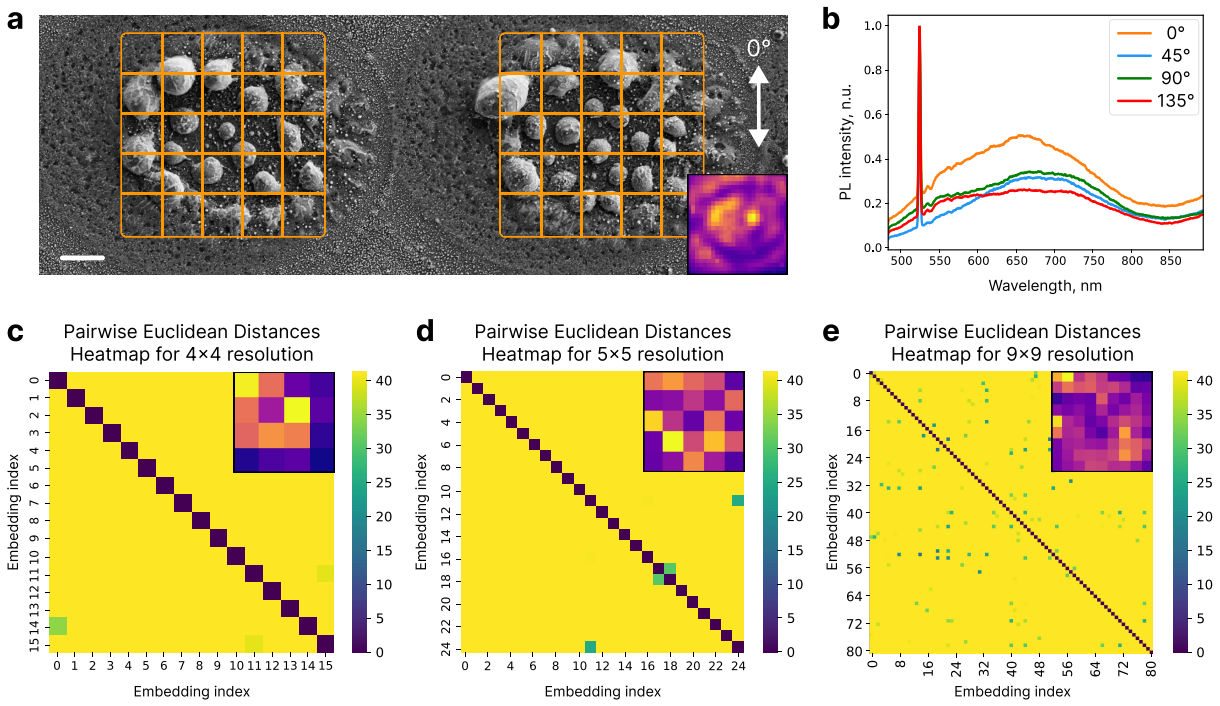
Supplementary Figure 14: **Finding the most appropriate value of clusters prescribed during the map clustering.** Distributions of the similarity indexes and pairwise matching maps for PUF labels encoded at **(a,d)** k=4, **(b,e)** k=5, and **(c,f)** k=6.



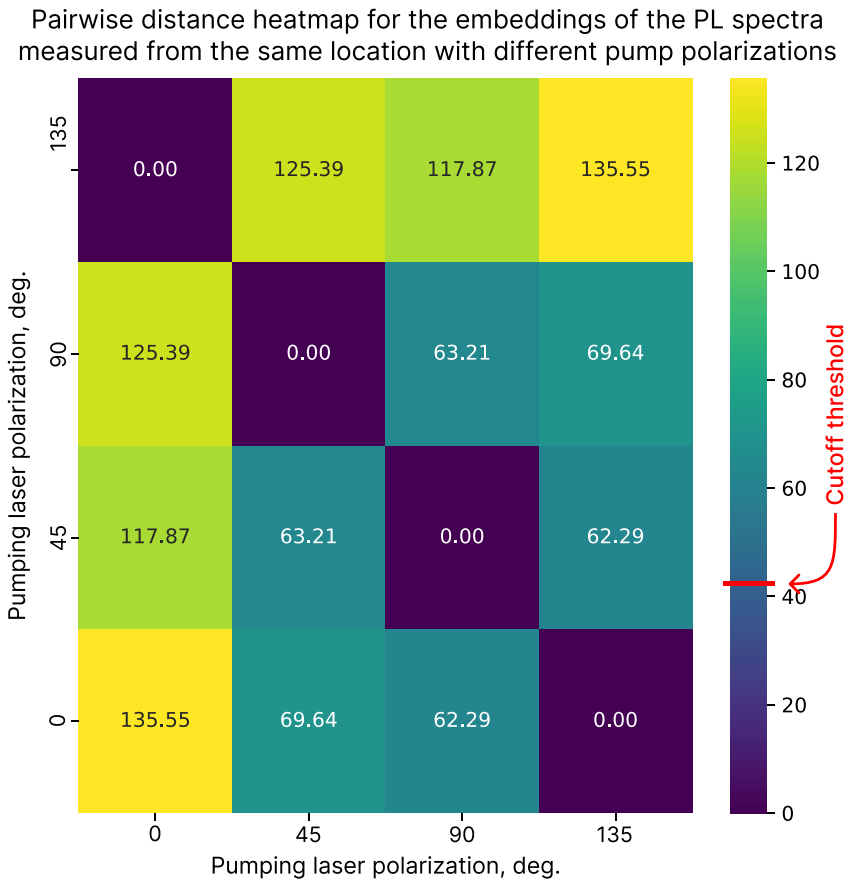
Supplementary Figure 15: **SEM imaging and high-resolution PL mapping of laser-printed QR codes.** **(a)** A photo of one of the samples taken using a bright-field microscope (scale bar is 35 um). **(b-c)** SEM images of the QR-code. The scale bars are 35 um and 10 um, respectively. **(d-f)** PL integrated intensity maps of QR-codes, measured with different resolutions: 120×120, 66×66, and 10×10.



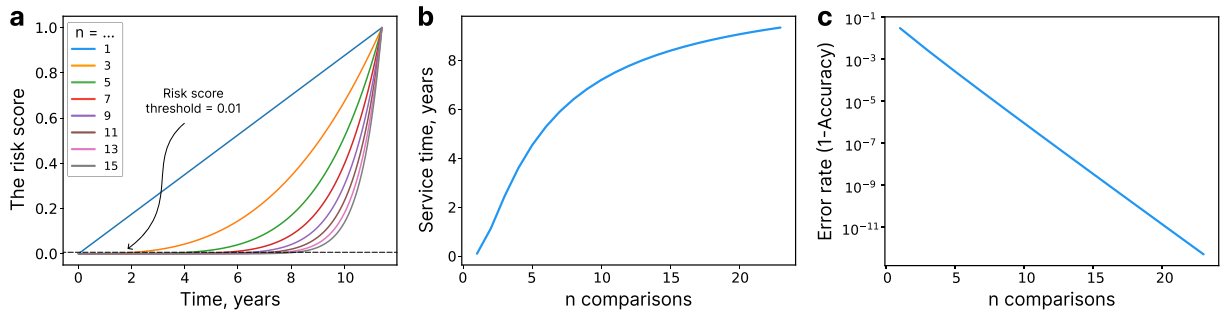
Supplementary Figure 16: **The process of PL image binarization made to estimate the encoding capacity of the second PUF protocol.** **(a)** Initial PL image. **(b)** The same image in the gray scale and **(c)** after binarization procedure relative to the threshold gray scale intensity of 30.



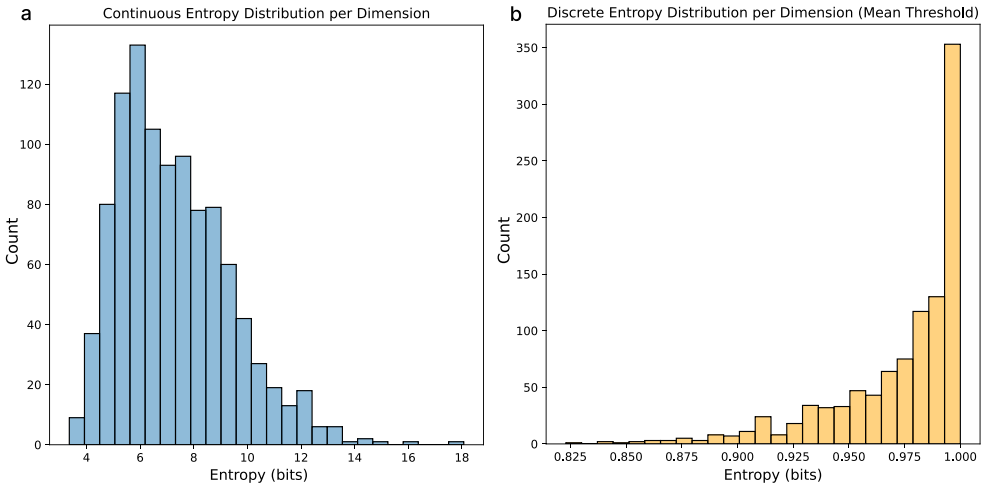
Supplementary Figure 17: **Evaluating the number of possible different PL responses that can be retrieved from one laser-printed microstructure.** **(a)** SEM image of two created microstructures, scale bar is 1 μm. The 5×5 grid defines the signal collection areas (with dimensions of 1 by 1 microns), and the double arrow indicates the 0° polarization axis. The insert: high-resolution PL intensity map of one of the structures. **(b)** The PL spectra measured from one of the $1\,\mu m \times 1\,\mu m$ areas at different polarizations of the pump laser beam. **(c-e)** Heatmaps of the Euclidean distances between embeddings, which were obtained after ML processing of PL maps of a single microstructure at different resolutions (4 by 4, 5 by 5, 9 by 9). The inserts represent the corresponding PL intensity maps. The maximum value of the color bars (41.3) is set in accordance with the threshold that determines the similarity between the two spectra in the developed model (refer to the main body of the paper for more information). The chosen grid resolution is 5×5.



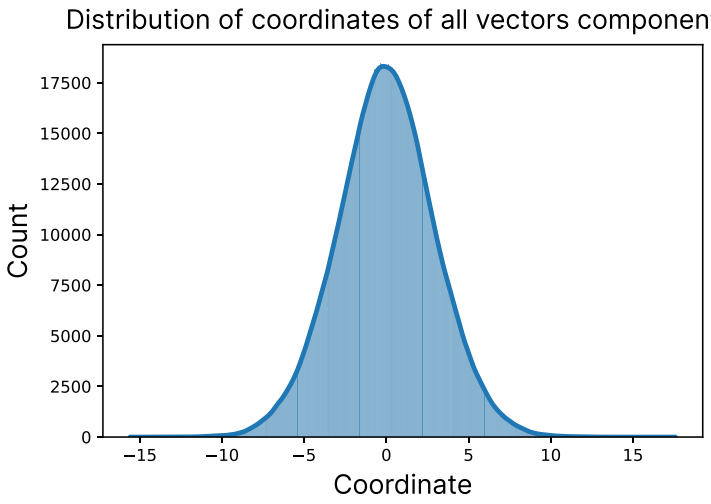
Supplementary Figure 18: **Pairwise distance heatmap for the embeddings of the PL spectra measured from the same location with different pump polarizations.** As can be seen, the obtained non-diagonal distances significantly exceed the cutoff value (**Supplementary Fig. 25**).



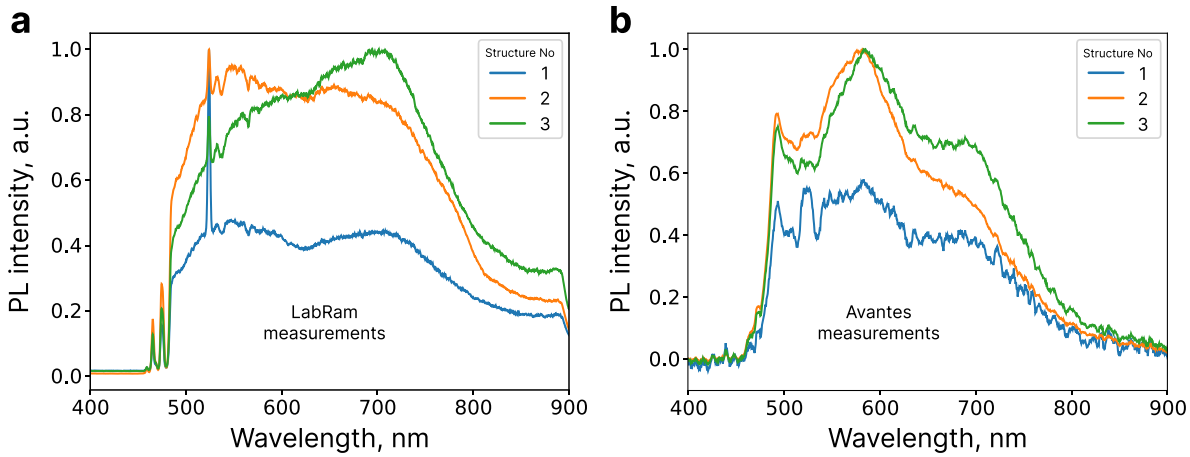
Supplementary Figure 19: **Characterizing the OTP token's performance depending on the number of spectra comparisons made during its verification.** **(a)** The dependence of the risk score (the probability of accidentally measuring the n spectra required for the future verification cycle as a result of continuous key measurement) on time for various n. The acceptable values of risk score should be lower than 0.01 (This probability threshold is chosen as an example). **(b)** The service time of the developed token as a function of the number of spectra comparisons performed to verify a user. **(c)** The dependence of the error rate when comparing several spectra on their number.



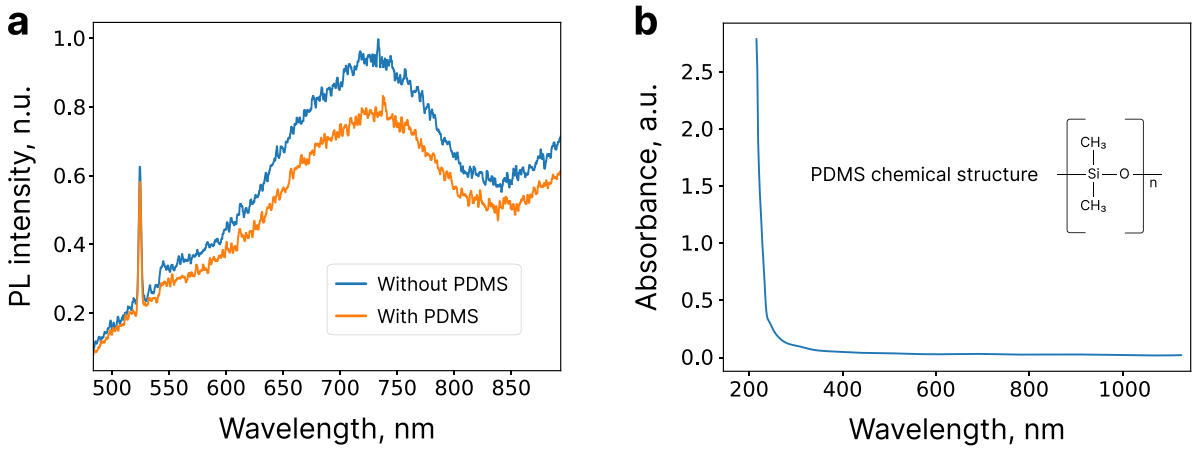
Supplementary Figure 20: **Results of the calculation of (a) continuous and (b) discrete entropy distributions per each embedding dimension**



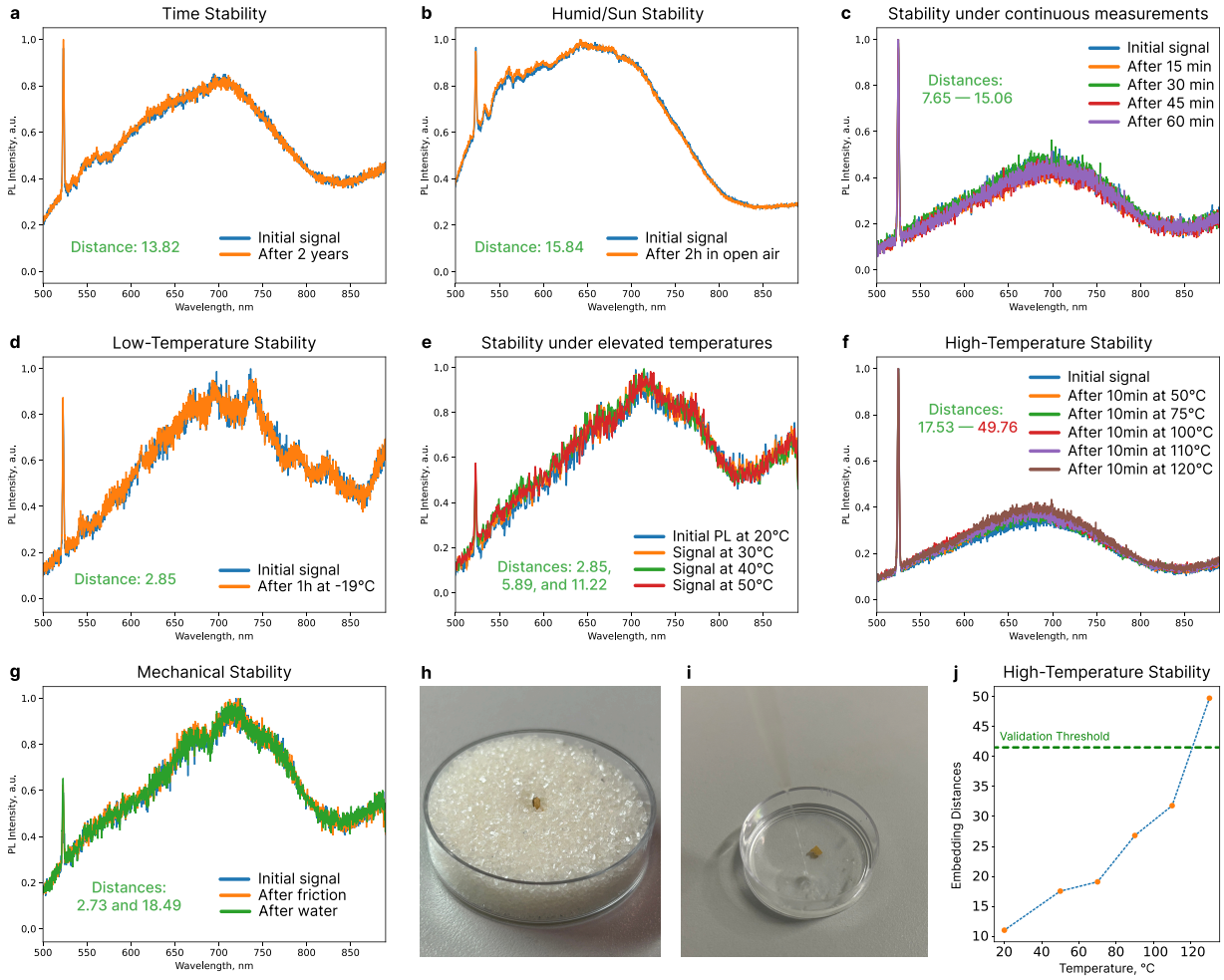
Supplementary Figure 21: **Distribution of the coordinates of all components of all embedding vectors obtained during ML model training.** As it seen, the majority of coordinates (95%) range from -6 to 6.



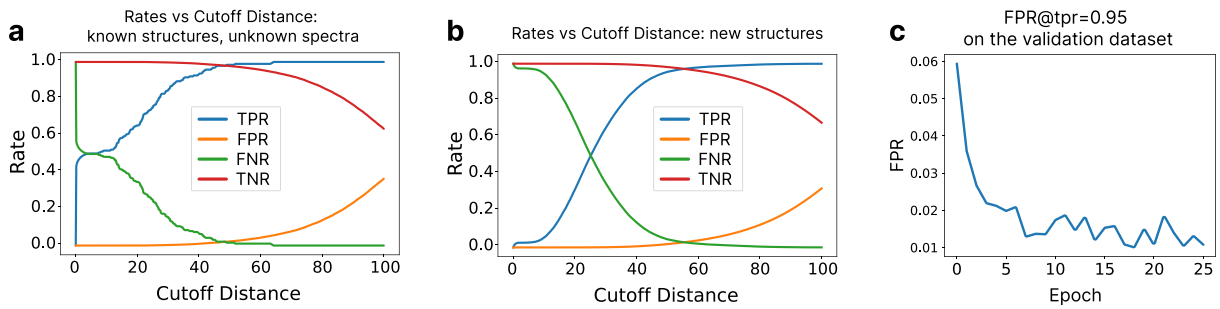
Supplementary Figure 22: **Testing an industrial optical fiber spectrometer for possible PL measurement.** PL spectra measured from different structures with **(a)** a laboratory Horiba LabRam HR spectrometer and **(b)** an optic-fiber spectrometer Avantes AvaSpec-2048. In both cases, the acquisition time was 1 second.



Supplementary Figure 23: **Considering the effect of the protective PDMS coating on the PL properties of the sample.** **(a)** PL spectrum measured from the same Au/Si structure before and after PDMS encapsulation of the sample. **(b)** Absorption spectrum of PDMS taken from ref.[41]



Supplementary Figure 24: **Testing environmental stability of the PL spectra-based PUFs. (a)** Time stability, **(b)** Humid/Sun stability, **(c)** Stability under continuous laser measurements, **(d)** Low-Temperature Stability, **(e)** Stability under elevated temperatures, **(f)** High-Temperature stability, and **(g)** Mechanical stability were investigated by measuring PL spectra before and after a certain experiment and calculating the distances between them (refer to the **Supplementary Note 19**). **(h, i)** Photos of mechanical stability experiments, where the sample was exposed to friction with granulated sugar and to the flow of deionized water, respectively (also see Supplementary Movie 1). **(j)** The temperature dependence of the distance calculated between the ML-generated embeddings for the initial and modified (or non-modified) PL spectra during high-temperature stability investigations.



Supplementary Figure 25: **Validation of the developed ML model.** Distributions of true positive (TPR), false positive (FPR), true negative (TNR), and false negative (FNR) rates depending on the value of cutoff distance built on the set of embeddings, obtained by ML processing new spectra from **(a)** previously known and **(b)** newly added structures. The optimal accuracy in both scenarios reaches about 97 percent. **(c)** The FPR at TPR=0.95 on the validation dataset as a function of the training epoch of the model.

Supplementary Table 1: Comparison of the quantum efficiency of silicon-based PL emitters between different works

Nanostructure	**QE**	**Excitation**	**Ref.**
BIC supporting Si/SiO2 cuboids	13.0%	720 nm	[42]
Si Nanospheres on Ag thin-film	8.6%	720 nm	[2]
Hybrid Au/Si particles	3.5%	1050 nm	This work
Si Nanospheres on Au thin-film	2.4%	720 nm	[1]
Si nanorod in Ω-shaped Au coating	1.4%	458 nm	[43]
Mie-resonant Si Nanospheres	1.2%	786 nm	[3]
Au/Si Nanoblobs	1.0%	720 nm	[1]
Au/Si Nanoparticles	0.1%	1050 nm	[44]

Supplementary Table 2: Summary of the randomness tests of binary sequences retrieved from the ML-generated embeddings of unique PL spectra

NIST statistical test	**Average Score**	**Pass percentage**
Monobit	0.638	100%
Frequency Within Block	0.273	98.5%
Runs	0.493	99.5%
Longest run	0.252	92.8%
Discrete Fourier Transform	0.444	97.2%
Non Overlapping Template Matching	0.762	95.2%
Serial	0.504	99.5%
Approximate entropy	0.438	97.8%
Cumulative sums	0.526	100%

Supplementary Table 3: The performance of several prominent optical PUFs in terms of critical and overall PUF size, storage density, encoding capacity, and acquisition time for a single optical measurement (see author notes below)

PUF system	Critical PUF sizes	Storage Density	EC	Acq. time	Comment
This work: Individual PL spectra with ML-driven verification	$10nm$ (CRS); $1\mu m$ (SAR)	3720 Bit/μm^2	$10^{1,120}$	1—3 s	The minimum structural unit of the PUF label consists of 25 signal acquisition sectors, has an overall size of 5x5 μm^2 and an EC of 10^{28000}
Si metasurface with Si-Er QDs[36]	$10nm$ (CRS); $2\mu m$ (SAR)	0.6 Bit/μm^2	10^{279}	1—200 s	A system with a size of 40x40 μm^2, which is read using standard optical and confocal Raman microscopy with a resolution of 20x20 pixels
Micropatterns of fluorescent nanofilms[45]	$20nm$ (CRS); $2\mu m$ (SAR)	8 Bit/μm^2	$10^{63,593}$	1 s	A microscale system (650x650 μm^2) with nanoscale z-axis variations, which is read using fluorescence and topography measurements (resolution: 325x325). The storage capacity is calculated on the optimistic assumption that the measured data is encoded with 32 independent bits (16 bits for fluorescence maps and 16 bits for topography maps), though in this work, the authors propose a lower estimate (2 bits)
Plasmonic (Gold) Nanojets[46]	$50nm$ (CRS); $2\mu m$ (SAR)	2.25 Bit/μm^2	$10^{1,693}$	—	Each PUF's unit represents the resonant Au submicrostructure, which exhibits a unique scattering color. The colors are encoded using RGB decomposition, where each color channel is digitized using 3 bits. The presented PUF (size: 50x50 μm^2) consists of 25x25 random structures, and its readout is conducted almost instantly using a dark-field microscope

Continued next

Supplementary Table 3 – continued

PUF system	Critical PUF sizes	Storage Density	EC	Acq. time	Comment
Gold-Silicon Structures[47]	$0.5\mu m$ (CRS); $8\mu m$ (SAR)	55 Bit/μm^2	$10^{1,452}$	1 s	The PUF's minimum unit (a single microstructure) has the size of 8x8 μm^2
Diamond microparticles[37]	$0.5\mu m$ (CRS); $2\mu m$ (SAR)	1.4 Bit/μm^2	$10^{1,014}$	up to 60 min	The PUF is encoded using the PL intensity of SiV centers in microdiamonds, which can be measured either in a static or in a dynamic regime (this is the reason for extensive readout durations). The EC is calculated for a PUF with a size of 100x100 μm^2, which is digitized at a resolution of 50x50 pixels
Lanthanide(III)-doped zeolites[13]	$1\mu m$ (SAR)	0.4 Bit/μm^2	10^{105}	20 ms/2 s	This PUF with a size of 30x30 μm^2 consists of randomly located lanthanides with distinct luminescence colors and is encoded via the analysis of its emission intensity profiles. An integration time of 1-2 s *per pixel* is required when the CCD imaging is used, while only 5-20 ms are needed when using the APD
Plasmonic nanoparticles[35]	$2\mu m$ (SAR)	8 Bit/μm^2	10^{243}	—	The PUF is based on the polarization-dependent scattering of gold nanoparticles, which is captured through the dark-field imaging. The EC is calculated for a 100-pixel area (each pixel can have one of 27 possible colors for 10 different polarization angles, though the correlation between these colors should be studied in more detail)

Continued next

Supplementary Table 3 – continued

PUF system	Critical PUF sizes	Storage Density	EC	Acq. time	Comment
Gap-enhanced Raman tags[48]	$2\mu m$ (SAR)	5 Bit/μm^2	10^{15051}	1 ms	The label (size: 100x100 μm^2) consists of ten types of randomly located SERS nanoparticles. Its Raman mapping is conducted (resolution: 50x50), and the resulting intensity maps are encoded with 2 bits at each pixel
Random fractal-enabled Au networks[39]	$2\mu m$ (SAR)	0.1 Bit/μm^2	10^{348}	—	The PUF has a circular form with a radius of 60 μm, though many different sizes and shapes may be achieved. The photo of its unique structural network is captured almost instantaneously with a portable mini-microscope. Each label is estimated to cost approximately 10^{-2} US$
This work: Direct PL imaging	$2\mu m$ (SAR)	0.09 Bit/μm^2	10^{141}	10 s	This PUF is encoded based on spatial distribution of PL intensity, which is captured by a standard digital camera with a 10x magnification lens. Acquisition time of 10 seconds corresponds to the overall time of making one camera shot of the whole label. The PUF is about $80\mu m$ in diameter
Micro-fingerprint of perovskite crystals[49]	$2\mu m$ (SAR)	0.06 Bit/μm^2	10^{271}	—	Each fingerprint has a size of about 125 μm. Its fluorescent microscopic photographs are divided into 30x30 pixels and encoded based on measured intensity using 1 bit per pixel. The fabrication cost is on the order of 10^{-5} US$ for one label

Continued next

Supplementary Table 3 – continued

PUF system	Critical PUF sizes	Storage Density	EC	Acq. time	Comment
Randomly distributed microdiamonds[50]	2.5μm (SAR)	0,16 Bit/μm^2	10^{3010}	—	A system of randomly distributed diamonds has a size of 250x250 μm^2. The authors conducted Raman mapping with a resolution of 100x100 and encoded the resulting intensity maps using 1 bit per pixel. The time required to collect the Raman signal is not provided
Phosphorescent organic crystal patterns[51]	5μm (SAR)	0.09 Bit/μm^2	$10^{7,000}$	0.1 s	The label with a size of 1x1 mm^2 represents an array of square (25x25 μm^2) fragments of phosphorescent organic crystals that are chaotically formed on MoS2. Image analysis of each fragment yields an encoding capacity of 10^{17}
Random Wrinkles[52]	5μm (SAR)	$6 \cdot 10^{-4}$ Bit/μm^2	10^{169}	—	Each fingerprint-like wrinkle has a size of about 215 μm, and its authentication is achieved by the identification of a microscopic image using the artificial intelligence analysis
This work: PL mapping and spectra decomposition	10μm (SAR)	0.02 Bit/μm^2	10^{54}	0.2 s	The PUF represents a 140x140 μm^2 QR code. Its PL response is digitized the a form of five 10x10 maps corresponding to different spectral PL features that are then encoded using a quinary number system
Scattering/absorbing microparticles[53]	15μm (SAR)	0,004 Bit/μm^2	10^{120}	—	These PUFs, measuring 3x3 mm^2, are authenticated using photos taken with a standard smartphone camera and processed with a resolution of 200x200

Continued next

Supplementary Table 3 – continued

PUF system	Critical PUF sizes	Storage Density	EC	Acq. time	Comment
Randomly distributed silk fibers[29]	$50\mu m$ (CRS); $1mm$ (SAR)	$5 \cdot 10^{-6}$ Bit/μm^2	10^{103}	—	This PUF has dimensions of 8x8 mm^2 and forms unique speckle patterns under LED illumination (the light wavelength and an angle of incidence may vary). Each pattern is captured with an image sensor and encoded in binary format with a resolution of 8x8
Randomly crystallized supersaturated solution[54]	$100\mu m$ (SAR)	$7 \cdot 10^{-8}$ Bit/μm^2	10^{163}	—	This PUF has dimensions of 4x2 mm^2 and forms unique speckle patterns upon laser beam irradiation. Each pattern is captured with a CMOS camera and encoded in binary format with a resolution of 32x32
Edible fluorescent proteins[55]	$500\mu m$ (SAR)	$5 \cdot 10^{-6}$ Bit/μm^2	10^{36}	5–60 s	The readout of this PUF (size: 6x6 mm^2) is achieved via fluorescence imaging of randomly located proteins. There are 4 types of microparticles with different excitation/emission lines, which results in 4 distinct fluorescence images for each PUF. The encoding resolution is 8x8
Injection-casted colloidal crystals[56]	$200\mu m$ (SAR)	$8 \cdot 10^{-5}$ Bit/μm^2	10^{2500}	0.1 s	The PUF size: 10x10 mm^2; it is captured with a standard camera and encoded in a decimal number system with a 50x50 resolution

Author notes: CRS — Characteristic Randomness Size; SAR — Signal Acquisition Resolution. Unless otherwise specified, SAR is of the same order as CRS. All the specified sizes and acquisition times serve as approximate indicators and should not be interpreted as exact values.

References

(1) He, X.; Liu, S.; Li, S.; Panmai, M.; Lan, S. Si/Au Hybrid Nanoparticles with Highly Efficient Nonlinear Optical Emission: Implication for Nanoscale White Light Sources. *ACS Appl. Nano Mater.* **2022**, *5*, 10676–10685.

(2) Xiang, J.; Panmai, M.; Bai, S.; Ren, Y.; Li, G.-C.; Li, S.; Liu, J.; Li, J.; Zeng, M.; She, J.; Xu, Y.; Lan, S. Crystalline Silicon White Light Sources Driven by Optical Resonances. *Nano Lett.* **2021**, *21*, 2397–2405.

(3) Zhang, C.; Xu, Y.; Liu, J.; Li, J.; Xiang, J.; Li, H.; Li, J.; Dai, Q.; Lan, S.; Miroshnichenko, A. E. Lighting up silicon nanoparticles with Mie resonances. *Nat. Commun.* **2018**, *9*, 1–7.

(4) Tiwari, A.; Samanta, R.; Chattopadhyay, H. Droplet solidification: Physics and modelling. *Appl. Therm. Eng.* **2023**, *228*, 120515.

(5) Stiffler, S. R.; Thompson, M. O.; Peercy, P. S. Transient nucleation following pulsed-laser melting of thin silicon films. *Phys. Rev. B* **1991**, *43*, 9851–9855.

(6) Starikov, S. V.; Lopanitsyna, N. Yu.; Smirnova, D. E.; Makarov, S. V. Atomistic simulation of Si-Au melt crystallization with novel interatomic potential. *Comput. Mater. Sci.* **2018**, *142*, 303–311.

(7) Larin, A. O.; Nominé, A.; Ageev, E. I.; Ghanbaja, J.; Kolotova, L. N.; Starikov, S. V.; Bruyère, S.; Belmonte, T.; Makarov, S. V.; Zuev, D. A. Plasmonic nanosponges filled with silicon for enhanced white light emission. *Nanoscale* **2020**, *12*, 1013–1021.

(8) Kolmogorov, A. Izv Akad Nauk SSSR. *Ser Mat* **1937**, *3*, 355–359.

(9) Bergmann, R. B.; Bill, A. On the origin of logarithmic-normal distributions: An analytical derivation, and its application to nucleation and growth processes. *J. Cryst. Growth* **2008**, *310*, 3135–3138.

(10) Teran, A. V.; Bill, A.; Bergmann, R. B. Time-evolution of grain size distributions in random nucleation and growth crystallization processes. *Phys. Rev. B* **2010**, *81*, 075319.

(11) Nakamura, S.; Hibiya, T. Thermophysical properties data on molten semiconductors. *Int. J. Thermophys.* **1992**, *13*, 1061–1084.

(12) Ho, C. Y.; Powell, R. W.; Liley, P. E. Thermal Conductivity of the Elements. *J. Phys. Chem. Ref. Data* **1972**, *1*, 279–421.

(13) Carro-Temboury, M. R.; Arppe, R.; Vosch, T.; Sørensen, T. J. An optical authentication system based on imaging of excitation-selected lanthanide luminescence. *Sci. Adv.* **2018**, *4*.

(14) Vidal, C.; Sivun, D.; Ziegler, J.; Wang, D.; Schaaf, P.; Hrelescu, C.; Klar, T. A. Plasmonic Horizon in Gold Nanosponges. *Nano Lett.* **2018**, *18*, 1269–1273.

(15) Wang, D.; Schaaf, P. Plasmonic nanosponges. *Advances in Physics: X* **2018**,

(16) Mazzone, V.; Falco, A. D.; Cruz, A.; Fratalocchi, A. Photonics based perfect secrecy cryptography: Toward fully classical implementations. *Appl. Phys. Lett.* **2020**, *116*.

(17) Horstmeyer, R.; Judkewitz, B.; Vellekoop, I. M.; Assawaworrarit, S.; Yang, C. Physical key-protected one-time pad. *Sci. Rep.* **2013**, *3*, 1–6.

(18) Di Falco, A.; Mazzone, V.; Cruz, A.; Fratalocchi, A. Perfect secrecy cryptography via mixing of chaotic waves in irreversible time-varying silicon chips. *Nat. Commun.* **2019**, *10*, 1–10.

(19) Anderson, R.; Kuhn, M. *Security Protocols*; Springer: Berlin, Germany, 2005; pp 125–136.

(20) Skorobogatov, S. P.; Anderson, R. J. *Cryptographic Hardware and Embedded Systems - CHES 2002*; Springer: Berlin, Germany, 2003; pp 2–12.

(21) Samyde, D.; Skorobogatov, S.; Anderson, R.; Quisquater, J.-J. *First International IEEE Security in Storage Workshop, 2002. Proceedings.*; IEEE, 2002; p 11.

(22) Matoba, O.; Nomura, T.; Perez-Cabre, E.; Millan, M. S.; Javidi, B. Optical Techniques for Information Security. *Proc. IEEE* **2009**, *97*, 1128–1148.

(23) Agrell, E. et al. Roadmap of optical communications. *J. Opt.* **2016**, *18*, 063002.

(24) Zhang, F.; Guo, Y.; Pu, M.; Chen, L.; Xu, M.; Liao, M.; Li, L.; Li, X.; Ma, X.; Luo, X. Meta-optics empowered vector visual cryptography for high security and rapid decryption. *Nat. Commun.* **2023**, *14*, 1–9.

(25) Pavlov, D.; Gurbatov, S.; Kudryashov, S. I.; Danilov, P. A.; Porfirev, A. P.; Khonina, S. N.; Vitrik, O. B.; Kulinich, S. A.; Lapine, M.; Kuchmizhak, A. A. 10-million-elements-per-second printing of infrared-resonant plasmonic arrays by multiplexed laser pulses. *Opt. Lett.* **2019**, *44*, 283–286.

(26) Kuchmizhak, A. A.; Porfirev, A. P.; Syubaev, S. A.; Danilov, P. A.; Ionin, A. A.; Vitrik, O. B.; Kulchin, Yu. N.; Khonina, S. N.; Kudryashov, S. I. Multi-beam pulsed-laser patterning of plasmonic films using broadband diffractive optical elements. *Opt. Lett.* **2017**, *42*, 2838–2841.

(27) Kudryashov, S. I.; Danilov, P. A.; Porfirev, A. P.; Saraeva, I. N.; Nguyen, T. H. T.; Rudenko, A. A.; Khmelnitskii, R. A.; Zayarny, D. A.; Ionin, A. A.; Kuchmizhak, A. A.; Khonina, S. N.; Vitrik, O. B. High-throughput micropatterning of plasmonic surfaces by multiplexed femtosecond laser pulses for advanced IR-sensing applications. *Appl. Surf. Sci.* **2019**, *484*, 948–956.

(28) Bassham, L. E.; Rukhin, A. L.; Soto, J.; Nechvatal, J. R.; Smid, M. E.; Leigh, S. D.; Levenson, M.; Vangel, M.; Heckert, N. A.; Banks, D. L. A Statistical Test Suite for Random and Pseudorandom Number Generators for Cryptographic Applications. *NIST* **2010**,

(29) Kim, M. S.; Lee, G. J.; Leem, J. W.; Choi, S.; Kim, Y. L.; Song, Y. M. Revisiting silk: a lens-free optical physical unclonable function. *Nat. Commun.* **2022**, *13*, 1–12.

(30) Cover, T. M.; Thomas, J. A. *Elements of Information Theory*; John Wiley & Sons, Inc., 2005.

(31) Gilbert, E. N. A comparison of signalling alphabets. *Bell System Technical Journal* **1952**, *31*, 504–522.

(32) Varshamov, R. R. Estimation of the number of signals in error-correcting codes. Reports of the Academy of Sciences. 1957; pp 739–741.

(33) Wiecha, P. R.; Lecestre, A.; Mallet, N.; Larrieu, G. Pushing the limits of optical information storage using deep learning. *Nat. Nanotechnol.* **2019**, *14*, 237–244.

(34) Gu, M.; Li, X.; Cao, Y. Optical storage arrays: a perspective for future big data storage. *Light Sci. Appl.* **2014**, *3*.

(35) Smith, J. D.; Reza, M. A.; Smith, N. L.; Gu, J.; Ibrar, M.; Crandall, D. J.; Skrabalak, S. E. Plasmonic Anticounterfeit Tags with High Encoding Capacity Rapidly Authenticated with Deep Machine Learning. *ACS Nano* **2021**, *15*, 2901–2910.

(36) Wang, K.; Shi, J.; Lai, W.; He, Q.; Xu, J.; Ni, Z.; Liu, X.; Pi, X.; Yang, D. All-silicon multidimensionally-encoded optical physical unclonable functions for integrated circuit anti-counterfeiting. *Nat. Commun.* **2024**, *15*, 1–11.

(37) Zhang, T. et al. Multimodal dynamic and unclonable anti-counterfeiting using robust diamond microparticles on heterogeneous substrate. *Nat. Commun.* **2023**, *14*, 1–11.

(38) Hultman, L.; Robertsson, A.; Hentzell, H. T. G.; Engström, I.; Psaras, P. A. Crystallization of amorphous silicon during thin-film gold reaction. *J. Appl. Phys.* **1987**, *62*, 3647–3655.

(39) Sun, N.; Chen, Z.; Wang, Y.; Wang, S.; Xie, Y.; Liu, Q. Random fractal-enabled physical unclonable functions with dynamic AI authentication. *Nat. Commun.* **2023**, *14*, 1–10.

(40) Esidir, A.; Kayaci, N.; Kiremitler, N. B.; Kalay, M.; Sahin, F.; Sezer, G.; Kaya, M.; Onses, M. S. Food-Grade Physically Unclonable Functions. *ACS Appl. Mater. Interfaces* **2023**, *15*, 41373–41384.

(41) Stankova, N. E.; Atanasov, P. A.; Nikov, Ru. G.; Nikov, R. G.; Nedyalkov, N. N.; Stoyanchov, T. R.; Fukata, N.; Kolev, K. N.; Valova, E. I.; Georgieva, J. S.; Armyanov, St. A. Optical properties of polydimethylsiloxane (PDMS) during nanosecond laser processing. *Appl. Surf. Sci.* **2016**, *374*, 96–103.

(42) Panmai, M.; Xiang, J.; Li, S.; He, X.; Ren, Y.; Zeng, M.; She, J.; Li, J.; Lan, S. Highly efficient nonlinear optical emission from a subwavelength crystalline silicon cuboid mediated by supercavity mode. *Nat. Commun.* **2022**, *13*, 1–9.

(43) Cho, C.-H.; Aspetti, C. O.; Park, J.; Agarwal, R. Silicon coupled with plasmon nanocavities generates bright visible hot luminescence. *Nat. Photonics* **2013**, *7*, 285–289.

(44) Makarov, S. V.; Sinev, I. S.; Milichko, V. A.; Komissarenko, F. E.; Zuev, D. A.; Ushakova, E. V.; Mukhin, I. S.; Yu, Y. F.; Kuznetsov, A. I.; Belov, P. A.; Iorsh, I. V.; Poddubny, A. N.; Samusev, A. K.; Kivshar, Yu. S. Nanoscale Generation of White Light for Ultrabroadband Nanospectroscopy. *Nano Lett.* **2018**, *18*, 535–539.

(45) Zhang, J.; Liu, Y.; Njel, C.; Ronneberger, S.; Tarakina, N. V.; Loeffler, F. F. An all-in-one nanoprinting approach for the synthesis of a nanofilm library for unclonable anti-counterfeiting applications. *Nat. Nanotechnol.* **2023**, *18*, 1027–1035.

(46) Lapidas, V.; Zhizhchenko, A.; Pustovalov, E.; Storozhenko, D.; Kuchmizhak, A. Direct laser printing of high-resolution physically unclonable function anti-counterfeit labels. *Appl. Phys. Lett.* **2022**, *120*, 261104.

(47) Ponkratova, E.; Ageev, E.; Trifonov, P.; Kustov, P.; Sandomirskii, M.; Zhukov, M.; Larin, A.; Mukhin, I.; Belmonte, T.; Nominé, A.; Bruyère, S.; Zuev, D. Coding of Non-Linear White-Light Luminescence from Gold-Silicon Structures for Physically Unclonable Security Labels. *Adv. Funct. Mater.* **2022**, *32*, 2205859.

(48) Gu, Y.; He, C.; Zhang, Y.; Lin, L.; Thackray, B. D.; Ye, J. Gap-enhanced Raman tags for physically unclonable anticounterfeiting labels. *Nat. Commun.* **2020**, *11*, 1–13.

(49) Liu, Y.; Zheng, Y.; Zhu, Y.; Ma, F.; Zheng, X.; Yang, K.; Zheng, X.; Xu, Z.; Ju, S.; Zheng, Y.; Guo, T.; Qian, L.; Li, F. Unclonable Perovskite Fluorescent Dots with Fingerprint Pattern for Multilevel Anticounterfeiting. *ACS Appl. Mater. Interfaces* **2020**, *12*, 39649–39656.

(50) Hu, Y.-W.; Zhang, T.-P.; Wang, C.-F.; Liu, K.-K.; Sun, Y.; Li, L.; Lv, C.-F.; Liang, Y.-C.; Jiao, F.-H.; Zhao, W.-B.; Dong, L.; Shan, C.-X. Flexible and Biocompatible Physical Unclonable Function Anti-Counterfeiting Label. *Adv. Funct. Mater.* **2021**, *31*, 2102108.

(51) Im, H.; Yoon, J.; Choi, J.; Kim, J.; Baek, S.; Park, D. H.; Park, W.; Kim, S. Chaotic Organic Crystal Phosphorescent Patterns for Physical Unclonable Functions. *Adv. Mater.* **2021**, *33*, 2102542.

(52) Chen, G.; Weng, Y.; Wang, W.; Hong, D.; Zhou, L.; Zhou, X.; Wu, C.; Zhang, Y.; Yan, Q.; Yao, J.; Guo, T. Spontaneous Formation of Random Wrinkles by Atomic Layer Infiltration for Anticounterfeiting. *ACS Appl. Mater. Interfaces* **2021**, *13*, 27548–27556.

(53) Arppe-Tabbara, R.; Tabbara, M.; Sørensen, T. J. Versatile and Validated Optical Authentication System Based on Physical Unclonable Functions. *ACS Appl. Mater. Interfaces* **2019**, *11*, 6475–6482.

(54) Kim, Y.; Lim, J.; Lim, J. H.; Hwang, E.; Lee, H.; Kim, M.; Ha, I.; Cho, H.; Kwon, J.; Oh, J.; Ko, S. H.; Pan, H.; Hong, S. Reconfigurable Multilevel Optical PUF by Spa-

tiotemporally Programmed Crystallization of Supersaturated Solution. *Adv. Mater.* **2023**, *35*, 2212294.

(55) Leem, J. W.; Kim, M. S.; Choi, S. H.; Kim, S.-R.; Kim, S.-W.; Song, Y. M.; Young, R. J.; Kim, Y. L. Edible unclonable functions. *Nat. Commun.* **2020**, *11*, 1–11.

(56) Wu, J.; Liu, X.; Liu, X.; Tang, Z.; Huang, Z.; Lin, W.; Lin, X.; Yi, G. A High-Security mutual authentication system based on structural color-based physical unclonable functions labels. *Chem. Eng. J.* **2022**, *439*, 135601.